RECOVERY OF THE SHEAR MODULUS AND RESIDUAL STRESS OF HYPERELASTIC SOFT TISSUES BY INVERSE SPECTRAL TECHNIQUES

A Dissertation

by

KUN GOU

Submitted to the Office of Graduate Studies of
Texas A&M University
in partial fulfillment of the requirements for the degree of

DOCTOR OF PHILOSOPHY

Approved by:

Chair of Committee,	Jay R. Walton
Committee Members,	Raytcho Lazarov
	Francis J. Narcowich
	Vikram Kinra
Department Head,	Emil J. Straube

December 2012

Major Subject: Mathematics

ABSTRACT

Inverse spectral techniques are developed in this dissertation for recovering the shear modulus and residual stress of soft tissues. Shear modulus is one of several quantities for measuring the stiffness of a material, and hence estimating it accurately is an important factor in tissue characterization. Residual stress is a stress that can exist in a body in the absence of externally applied loads, and beneficial for biological growth and remodeling. It is a challenge to recover the two quantities in soft tissues both theoretically and experimentally. The current inverse spectral techniques recover the two unknowns invasively, and are theoretically based on a novel use of the intravascular ultrasound technology (IVUS) by obtaining several natural frequencies of the vessel wall material.

As the IVUS is interrogating inside the artery, it produces small amplitude, high frequency time harmonic vibrations superimposed on the quasistatic deformation of the blood pressure pre-stressed and residually stressed artery. The arterial wall is idealized as a nonlinear isotropic cylindrical hyperelastic body for computational convenience. A boundary value problem is formulated for the response of the arterial wall within a specific class of quasistatic deformations reflexive of the response due to imposed blood pressures. Subsequently, a boundary value problem is developed from intravascular ultrasound interrogation generating small amplitude, high frequency time harmonic vibrations superimposed on the quasistatic finite deformations via an asymptotic construction of the solutions. This leads to a system of second order ordinary Sturm-Liouville problems (SLP) with the natural eigenfrequencies from IVUS implementation as eigenvalues of the SLP. They are then employed to reconstruct the shear modulus and residual stress in a nonlinear approach by inverse spectral

techniques.

The shear modulus is recovered by a multidimensional secant method (MSM). The MSM avoids computing the Jacobian matrix of the equations and is shown to be convenient for manipulation. Residual stress is recovered via an optimization approach (OA) instead of the traditional equation-solving method. The OA increases the robustness of the algorithms by overdetermination of the problem, and comprehensive tests are performed to guarantee the accuracy of the solution. Numerical examples are displayed to show the viability of these techniques.

DEDICATION

For the love and encouragement of my parents Mr. Qiangui Gou and Mrs. Kaicui Liu, and my wife Lijuan Xue. Also to my daughters Rebecca Joy Gou and Hannah Grace Gou.

ACKNOWLEDGEMENTS

First of all, special thanks is presented to my academic adviser Prof. Jay R. Walton. His outstanding researches on interdisciplinary areas properly match my research philosophy that "Applied Math should be applied directly to real-world problems". With his guidance, I have gained valuable training in doing crossdisciplinenary researches. He taught me how to analyze problems and resolve difficult issues effectively and smartly. I also appreciate his time in discussing with me for my research projects so that I could advance my research more smoothly. His guidance on how to write high-quality paper is a life-time treasure for me. Moreover, his personal care to me as a friend will remain as a long-lasting memory in my mind.

I express my deep gratitude to my committee members, Prof. Raycho Lazarov, Francis Narcowich and Vikram Kinra. Prof. Raycho Lazarov's class on Numerical Analysis built a foundation for my computational ability. I am also deeply impressed by his unselfish assistance in my research. Prof. Francis Narcowich' two classes Applied Analysis and Harmonic Analysis further strengthened my analytical ability in applied math. His generosity in discussing with me for my research problem also stimulated my thinking in problem solving. Prof. Vikram Kinra, from Department of Aerospace Engineering, has inspired me to analyze problems from different perspectives. I am also lucky to take his class on Fracture Mechanics, which leads me to develop interests in this area.

I am thankful to Prof. Peter Howard, now the associate department head for graduate programmes. His love for graduate students makes us relieved from our status as students. His patience in dealing with our requests is highly appreciated. His clear and organized teaching in the class for Partial Differential Equations also

sets an excellent example for us.

I thank Ms. Monique Stewart for her whole-hearted service to graduate students. Her work to us made our studies much easier.

I am also thankful to other faculty members and staff in the Department of Mathematics. Together, they make the department a home for me to stay for so many years. They have witnessed my growth throughout the years and will stay in my memory.

NOMENCLATURE

IVUS	Intravascular ultrasound technology
SLP	Sturm-Liouville problem
MSM	Multi-dimensional method
OA	Optimization approach

TABLE OF CONTENTS

LIST OF FIGURES

LIST OF TABLES

TABLE Page

1. INTRODUCTION

Soft tissues are composite materials with constitutions and structure continually varying corresponding to tissue and mechanical environment [1]. They also display the potential to undergo large deformations and still restore back to the initial configuration when unloaded. The mechanical behavior of biological soft tissue plays a vital role in maintenance of health and growth for living bodies. However, modeling the mechanical behavior in soft tissue can be a very challenging task. The research in the dissertation focuses on modeling the mechanics of the wall of large muscular arteries in human or animal models. While the mechanics of the arterial wall is a subject extensively developed in a vast literature [10, 11, 16, 17, 22], there are still many critical issues yet to be fully resolved. Among these are reliable techniques for devising and fitting robust models capable of reproducing both the in vivo and in vitro mechanical behavior of the arterial wall.

It is now well-established that mechanical factors play a central role in understanding the mechanobiology of both healthy and diseased arteries [17]. For example, mechanical factors such as inner-wall shear stress and within-the-wall tensile stresses have major influence on growth and remodeling of the arterial wall, and the initiation and growth of atherosclerotic lesions. Attaining a deeper understanding of the mechanobiology of arteries requires the ability to more accurately estimate the stresses the arterial wall experiences in vivo than current techniques allow.

Based on the framework established in [27], the dissertation focuses on developing mathematical inverse spectral techniques to numerically recover the spatially nonhomogeneous shear modulus and residual stress of the arterial wall by making a non-traditional use of intravascular ultrasound (IVUS) technique for imaging ar-

teries particularly. The shear modulus or modulus of rigidity, defined as the ratio of shear stress to the shear strain, is a quantity for measuring the stiffness of materials. Estimating it accurately is a significant factor in tissue characterization. Unfortunately, the identification of it in vivo for arterial wall displays a difficulty in recent studies [22]. Meanwhile, residual stress is a stress that exists in a body in the absence of externally applied loads. This means that even in the unloaded state, there is still stress in the tissues, which is steady and at an equilibrium state with its surroundings, contributing to the biological modification. These two quantities are reconstructed by different inverse spectral techniques.

1.1 Project Background

The research in the dissertation is part of the long range project for distinguishing the safe atherosclerotic plaques from vulnerable ones. Atherosclerosis is one of the most fatal diseases of the muscular cardiovascular system. It is a disease in which plaques build up inside the inner wall of muscular arteries due to various biological processes [4, 21], through which the arterial wall thickens as a result of build up of cholesterol and other fatty materials inside the interior surface of the wall. A soft core plaque is initially formed, and as time progresses, a fibrous layer builds up on it due to various biological processes such as calcification, cell necrosis, mural thrombus, or hemorrhage [4, 21]. This process takes place over a long period of time, and the extent and severity of the disease depend on the thickness of the calcified fibrous layer. A vulnerable or unsteady plaque is one that the later formed cover is not thick enough so as to cause the plaque to rupture suddenly leading to fatal diseases like acute myocardial infarction, sudden cardiac death etc. [21]. On the contrary, the safe or stable plaque is one that the cover is thick enough to prevent a sudden rupture of the inner core. Different kinds of plaques possess different material stiffnesses

and residual stress distributions. Understanding the shear modulus and residual stress distribution in atherosclerotic plaques could be key aspects for discrimination between the two kinds of plaques. This dissertation focuses on studying the shear modulus and residual stress distribution in healthy arteries, from which one can further understand it in atherosclerotic lesions.

1.2 A Novel Use of IVUS

Discovery of the plaques in a timely manner is essential for proper cure of the disease. One of the frequently used medical technique is IVUS for locating and characterizing obstructions inside blood vessels [43]. It is an invasive procedure in which a catheter is inserted into the vessel. On the distal tip of the catheter is an extremely miniaturized transducer which sends small amplitude, high frequency ultrasound waves to the arterial wall and records its echo. The echo is transformed back to the other end of the catheter which is connected to a computerized ultrasound processor that generates detailed images of the interior arterial wall. The images allow one to see from inside out the cross sectional view of the artery in vivo, and thus detect atherosclerotic plaques, quantify the morphology of them [48], and analyze structure and composition of the obstructions. The IVUS images of the calcified, fibrous part of the plaques are generally brighter and more homogenous than that of the softer, fatty ones which absorb more ultrasound wave [12, 30] (See Figure 1.1 for a schematic view of IVUS cathter insider an artery and a sample IVUS image for atherosclerotic plaque). By the IVUS image analysis and high-order statistical texture-based algorithms, one can understand the plaque composition [49].

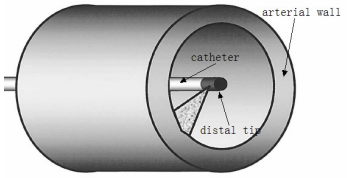

(a) A schematic display of IVUS catheter operating inside an artery emitting ultrasound wave (from [28]).

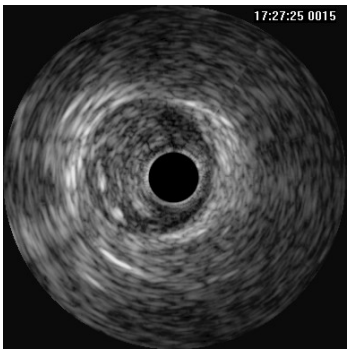

(b) A sample IVUS image of inner artery with atherosclerotic plaque (from myheartpartner.com).

Figure 1.1: Operation of IVUS equipment inside an artery and a sample IVUS image.

However, for more advanced demands to discriminate the stable plaques from unstable ones more accurately, the results from IVUS are unsatisfactory [54, 55]. Based on its operational principle, a novel use of the IVUS technique is conceived for more accurate discrimination. Under the IVUS interrogation, the ultrasound wave propagates through the vessel wall causing the wall to vibrate in a nanoscale due to its periodic force imposed on the prestressed and residually stressed arterial wall. One can control the frequency of the ultrasound wave to produce arterial wall resonances. Several natural frequencies of the wall tissue can be obtained, which are close to the wave frequencies creating resonances. These eigenfrequencies are crucial information of the plaque tissues, which can be explored for better distinguishment of stable and vulnerable plaques. Towards this aim, this research makes use of the natural eigenfrequencies to calculate the shear modulus and residual stress for understanding the stiffness and mechanical distribution of the tissues.

1.3 Tissue Characterization and Simplifications

Soft tissue, in general, or an arterial wall, in particular, exhibits complex mechanical behavior. Among the significant complications are: highly nonlinear stress-deformation response; anisotropy; inhomogeneity; time-dependent response; active and passive response; pre-stress and residual stress; and complex in vivo boundary conditions. Devising a testing program and modeling setting through which the mechanical behavior of arteries can be determined that takes account of this full range of complexity is a daunting task, even more so if the program is to be applicable both in vivo and in vitro. It is proposed to base a mechanical characterization testing procedure on a nondestructive, inverse spectral, ultrasound interrogation technique. The inverse spectral, ultrasound approach proposed herein is in contrast to conventional soft-tissue elastography and conventional nondestructive evaluation methods as applied to traditional structural engineering materials. In particular, it makes fundamental use of the finite strain, nonlinear response of the material to pre-stresses resulting from quasistatic loading upon which infinitesimal strain, ultrasound induced, harmonic waves are superimposed.

In the idealized modeling of arterial wall, some main assumptions have been made. First, though arterial wall is experimentally shown to be anisotropic [11, 46], it is assumed to be isotropic for an initial simplified formulation of the mechanical framework and inverse spectral techniques, and anisotropy will be incorporated in subsequent studies for more practical modeling. Second, some computational results reveal that arterial wall is slightly noncircular [41], but circularity assumption can be a reasonable approximation for typical arteries, and this trend is followed. Third, to avoid end boundary effects, an artery is assumed to be an infinitely long cylindrical tube. Lastly, the arterial wall is thought to be prestressed purely by blood pressures

in the mechanical framework and other factors are excluded like the influence from the outer tissues. This assumptions, though ignoring some elements, grasp the main aspects of the tissue situation and helpfully make the mathematical modeling and its computation more tractable.

1.4 Main Content and Structure of the Dissertation

In the modeling framework, two kinds of boundary value problems are established according to two categories of deformations respectively. The first category contains the quasistatic deformations of the residually stressed arterial wall subjected to blood pressures. The other one relies on the IVUS interrogation generating small amplitude, time harmonic ultrasound vibrations superimposed upon the quasistatic large deformations. These boundary value problems are transformed to Sturm-Liouville problems (SLP), of which the eigenvalues are from the natural frequencies generated by IVUS implementation. Inverse spectral techniques are developed to reconstruct the shear modulus and some components of the residual stress tensor. It is important to note that, unlike other harmonic analysis approaches which use a single blood pressure for as many eigenfrequencies as needed [23], the approaches applied in this dissertation are based on formulating a system of boundary value problems corresponding to different blood pressures, and using several lower-mode eigenfrequencies as input data from each of the blood pressures to construct the shear modulus and residual stress. Utilization of several blood pressures and a few lower-mode eigenfrequencies for each of them makes our approaches *nonlinear* and the results more accurate, since more blood pressures involved produce an over-estimation for the solution, and the lower-mode eigenfrequencies can be more easily estimated experimentally with higher accuracy.

The inverse spectral techniques are realized by MSM for reconstruction of the

shear modulus and by OA for recovery of residual stress [28,37]. Many other inverse spectral techniques are developed only for forms of simple SLP, and the solutions are obtained through solving a system of equations or forming iterations by principle of fixed point theorem [44,56,57]. However, the unknowns in a complicated biological problem are intricately involved in the SLP, the solutions of which are only locally unique and many other perturbational solutions exist densely around the real ones. What makes things worse is that the real solutions are indistinct from their surroundings. These difficulties make the traditional approaches easily divergent, or if used, astonishing quantity of computation is needed. The techniques in this dissertation avoid these obstacles due to their more flexible and effective algorithms.

The remainder of the dissertation is organized as follows. In Chapter 2, introduction to Green elasticity and SLP is presented for a better understanding of the mechanical and mathematical theory applied in the dissertation. In Chapter 3, it illustrates how residual stress is involved with natural Cauchy stress in soft tissues. The tissue constitutive model is also given under the simplifications provided in the introduction. This chapter also contains the construction of boundary value problems for quasistatic deformation and vibration caused deformation via an asymptotic expansion technique for modeling the response of an arterial wall to ultrasound interrogation through the superposition of small amplitude, time harmonic waves upon a large, quasistatic deformation. In Chapter 4, complete algorithms for reconstruction of the shear modulus and residual stress are shown. Numerical examples with tables and plots are presented to show the viability of these algorithms. The last chapter contains discussions, summary of contributions and future research plans. From the appendix, readers can find other fundamental algorithms utilized in the inverse spectral techniques.

2. PRELIMINARIES

2.1 Basics of Green Elasticity

This section briefly reviews several main concepts of Green elasticity employed in this dissertation: deformation of a material object, the Cauchy stress, Piola-Kirchhoff stress, response function, strain-energy function etc.

For a material body embedded in a 3-dimensional Euclidian space, two configurations are considered. One is the current configuration denoted as β_t dependent on the current time t. The other one is a particular configuration β (the time subscript is omitted) for some fixed time t_0 as the reference configuration. The coordinate of any point in β is labeled by X. The coordinate of the same point in β_t is x. If it is the deformed configuration not the deformation history that is significant such that time can be neglected, the *deformation or motion* mapping from β to β_t is set to be

$$x = \chi(X), \tag{2.1}$$

where χ is a set of invertible functions.

The deformation gradient tensor F is calculated by the formula

$$F = \nabla\chi, \tag{2.2}$$

where ∇ is the gradient operator. The cartesian component of F is given by $F_{ij} = \frac{\partial x_i}{\partial X_j}$, for $i, j = 1, 2, 3$.

The *Cauchy stress tensor* T is a second order tensor defined to describe the stress distribution of each point in the current configuration. If for some material body, the Cauchy stress is a function of F and X as $T = \widehat{T}(X, F)$, then such material is

said to be *elastic* and $\widehat{T}$ is called the *response function*. Furthermore, if as $F = I$, $T = 0$, then β is called a *natural configuration*. Otherwise, the material body is said to be residually stressed and the residual stress distribution is $\widehat{T}(X, I)$.

Practically, Cauchy stress is hard to be measured since information for the current configuration can not be obtained in advance easily. *Piola-Kirchhoff stress* tensor S is defined in the reference configuration for a convenient measurement as

$$S = JTF^{-T}, \tag{2.3}$$

where $J = det(F)$, i.e. the determinant of F, and F^{-T} means the inverse transpose of F. One can also define the response function for S to be $S = \widehat{S} = J\widehat{T}F^{-T}$.

Furthermore, an elastic material is called *hyperelastic* if for some scalar function $\widehat{W}(F)$ called *strain-energy function* satisfying *principle of material frame indifference* such that

$$\widehat{S}(F) = \frac{\partial \widehat{W}(F)}{\partial F}. \tag{2.4}$$

For hyperelastic material, $\widehat{T}(F) = \frac{\partial \widehat{W}(F)}{\partial F} F^T J^{-1}$.

Lastly, the *equations of motion* derived from balance of linear momentum of the material body are

$$\mathrm{Div}S + \rho b = \rho \ddot{\chi}, \tag{2.5}$$

where Div is the divergence operator on β, ρ is the point-wise density of the material body, b is the body force per unit mass, and $\ddot{\chi}$ denotes the second derivative of χ with respect to time. (2.5) is subjected to appropriate boundary or initial conditions. In this dissertation, only the soft tissue in its final configuration is studied, so b and $\ddot{\chi}$ are taken to be zero.

2.2 Introduction to Sturm-Liouville Problem

2.2.1 Direct Sturm-Liouville Problem

The general form of the classical SLP is defined as

$$-\frac{d}{dx}\Big(p(x)\frac{du(x)}{dx}\Big) + q(x)u(x) = \lambda\omega(x)u(x), \tag{2.6}$$

where the coefficients $p(x), q(x)$ and $\omega(x)$ are known real functions. This equation is defined on a finite or infinite interval $a < x < b$. Two boundary conditions are defined at the two ends a and b appropriately. λ is unknown to us. Not all real or complex values for λ can make the equation generate a nontrivial solution. It is known that only a discrete set of values can do so. We call any such value an eigenvalue of the SLP. Under most cases they are real, but there are also cases under which they can be complex [47]. The nontrivial solution corresponding to an eigenvalue is called an eigenfunction of the problem.

Though specifically defined, SLP can be easily derived from second order ordinary differential equations. Set a linear equation of the form

$$F(x)u'' + Q(x)u' + G(x)u = \lambda E(x)u \quad \text{for} \quad x \in [a, b], \tag{2.7}$$

where $F(x) \neq 0$ for any $x \in [a, b]$. Dividing this equation by $F(x)$ and then multiplying it by $e^{\int (Q/F)dx}$ yield

$$-(e^{\int (Q/F)dx}u')' + (-\frac{G}{F}e^{\int (Q/F)dx})u = -\lambda(\frac{Ee^{\int (Q/F)dx}}{F})u, \tag{2.8}$$

which is the form of (2.6).

The $regularSLP$ is defined as follows.

Definition 2.3 *The SLP (2.6) is regular if*

1. *a and b are finite;*

2. *$p(x)$, $q(x)$ and $\omega(x)$ are defined on $[a, b]$. They are all piece-wise continuous with at most finite jumps of discontinuities;*

3. *$p(x)$ and $\omega(x)$ are strictly positive on the domain, i.e. $p(x)$, $\omega(x) > 0$, for any $x \in [a, b]$;*

4. *Boundary conditions are of the form*

$$a_0 u(a) + a_1 u'(a) = 0 \qquad b_0 u(b) + b_1 u'(b) = 0, \tag{2.9}$$

where a_0, a_1, b_0 and b_1 are all real constants satisfying $a_0^2 + a_1^2 \neq 0$ and $b_0^2 + b_1^2 \neq 0$.

We define an inner-product for any two real functions u and v as $< u, v >= \int_a^b uv\omega dx$, where ω is the same as in (2.6). Set an operator $L = \frac{1}{\omega(x)}[-\frac{d}{dx}(p(x)\frac{d}{dx}) + q(x)]$, where $a \leq x \leq b$. The operator L with boundary conditions of regular SLP is self-adjoint with respect to the inner product. Namely, $< Lu, v >=< u, Lv >$. For a regular SLP, we have the following theorem [47].

Theorem 2.4 *For a regular SLP*

1. *The eigenvalues are simple. Namely, each eigenvalue generates only one linearly independent eigenfunction;*

2. *The eigenvalues can be ordered to be a sequence which tends to positive infinity. That is to say, we can put all the eigenvalues in an order $\lambda_0 < \lambda_1 < \lambda_2 < \lambda_3 < \cdots$.*

2.4.1 Inverse Sturm-Liouville Problem

For a regular SLP, given the functions $p(x)$, $q(x)$, $\omega(x)$ and the boundary conditions, the eigenvalues and corresponding eigenfunctions can be found. This is called the *direct problem*. Reversely, if the eigenvalues are given, one is able to recover the

coefficients p, q and w under certain conditions. This is called the *inverse SLP* or the *inverse spectral problem*. The inverse SLP has wide applications in areas like physics and engineering.

For the inverse SLP, the regular SLP is further simplified to reduce the three coefficient functions to only one so that we can find an effective algorithm for it. The usual way is by a transformational method, and the one frequently used is the *Liouville transform* [47]. It includes change of variable and domain, and transformation of coefficients from the original form. After that, we can get the *canonical form* or *Schrödinger form* of the SLP as

$$-\frac{d^2}{dt^2}v(t) + N(t)v(t) = \sigma v(t), \tag{2.10}$$

with boundary conditions $v'(0) - hv(0) = 0$ and $v'(1) + Hv(1) = 0$.

The inverse spectral problem is formulated in several ways [8,44,56], two of which are listed below:

Two-spectrum case: Two sets of eigenvalues $\{\sigma_n^{(1)}\}_{n=0}^{\infty}$ and $\{\sigma_n^{(2)}\}_{n=0}^{\infty}$ are given for the canonical form (2.10) from two different pairs of known boundary conditions and we recover $N(t)$.

Partially known $N(t)$ case: $N(t)$ is known over at least half of the interval [0, 1], say $[\frac{1}{2}, 1]$, and a single set of eigenvalues $\{\sigma_n\}_{n=0}^{\infty}$ is given. We recover the other part of $N(t)$ on the interval $[0, \frac{1}{2})$. See [39] for a computational method for this particularity.

The inverse spectral method for the biological model we establish is of a different type. It is called the *shooting method for inverse spectral problem*. The unknown function to be recovered is approximated by cubic spline functions, and it appears both in the coefficients and the boundary conditions of the SLP. Moreover, the

coefficients of the SLP depend on another function r_0 which can only be solved numerically from a differential equation also related to the unknown function. The details are presented in Chapter 4.

3. FORMULATION OF BOUNDARY VALUE PROBLEMS

3.1 Interaction of Residual Stress in the Tissue

Biomechanically, the arterial wall is under the effect of both pre-stress and residual stress. Pre-stress in a material body arises from external loads whereas residual stress exists in the absence of external loads. Bergel was one of the first to observe residual stress in arteries. He found that when an artery is split open longitudinally, it will unroll itself [25]. Studies show that residual stress in arteries is caused by growth and remodeling of the tissues to make the cells in the arterial wall optimize their biomechanical effect and maintain compatible growth of tissues [36, 38]. As the artery becomes abnormal, residual stress contributes to modifying the structure and cell composition of the tissues to restore back to the normal biomechanical condition of the vessels [26, 35]. It is also developed to avoid stress gradient among the multiple layers of arteries for a uniformity of stress distribution [40, 52, 53]. Consequently, failure to incorporate residual stress in the biomechanical analysis of the arteries will produce false predictions for the internal stress distribution of the vessel wall and cell biological signalling response.

From the perspective of material, residual stress in artery stems from interactions among time, temperature, deformation and microstructure [31]. Correspondingly, the arteries are shown to display three levels of interactions between residual stress and the tissue: micro-level, meso-level and macro-level [29]. In the micro-level, residual stress comes from local interactions among constituents of the tissue like fibers, cell. Greenwald et al. showed that residual stress relies mainly on intramural elastin [40]. In the meso-level, the nonhomogeneities of the tissue's microstructure and constituents's compositions may alter the residual stress. Zeller and

Skalak showed that residual stress has different forms in different ingredients [42]. In elastin, it shows to be residual tension while in collagen, it develops into residual compression. In the macro level, residual stress can also be modified by temperature and the kinematical constraints superimposed on the tissue's boundary producing extra internal loading. Due to the widespread origination of residual stress, it is very difficult to devise experiments to obtain a complete distribution of it in all the three levels.

Fung's paradigm is the pioneering one among the many methods. This technique makes a single radial cut through an excised, unloaded arterial ring segment [6,9,26]. The ring segment springs open to minimize its stored energy by relieving the residual stress. One can conclude that, in order that such opening occurs, it is compressive stress in inner wall and tensile stress in the outer wall as a result of inhomogeneous distribution of residual stress, so that the wall is internally balanced. It is assumed that residual strains are constant circumferentially in the ring. By measuring the inner and outer circumferences of the ring before and after cutting, one can estimate the stretch ratio for the inner and outer surface respectively. This establishes an approach for calculating the residual stress state indirectly.

This approach bears a few limitations. First, it is obvious that one cutting can not relieve all the residual stress by the fact that extra cutting makes the ring segment open more. This results from the micro-level of the interaction between residual stress and tissue. Second, the magnitude of opening angle is affected by internal and external conditions like temperature, hemodynamic load, position of cutting etc. Fung's paradigm can not incorporate these macro-level effects. Last, the reference configuration from the cut with openings can not evolve to the intact ring segment without topological change, since the two faces of the cut map to a common internal surface of the intact arterial segment. This brings difficulties for theoretical

utilization of the measurement.

Actually, not only Fung's paradigm but any other experimental method can not fully reconstruct the residual stress distribution in the arteries. Using analytical approaches to determine residual stress distribution is highly appreciated in understanding the mechanical effect of arterial wall. Among these is the virtual stress free configuration invented by Hoger et al. [13, 14, 18, 32]. The configuration used in [33] is followed in this dissertation to estimate residual stress analytically.

3.2 Residual Stress in Stress Tensor and the Constitutive Model

In order to incorporate residual stress in the model analytically, we assume the total Cauchy stress is an additive form of the natural Cauchy stress and residual stress as

$$T = \widehat{T}_N(F) + \frac{1}{J} F\tau F^T, \tag{3.1}$$

where τ is the residual stress tensor, and $\widehat{T}_N(F)$ is the natural response function in the sense that it gives the deformational behavior in the absence of residual stress. We remark that $\frac{1}{J} F\tau F^T$, the contribution of residual stress to the total Cauchy stress, is chosen so as to satisfy material objectivity.

By the assumption for Cauchy stress in Equation (3.1), total Piola-Kirchhoff is

$$S = \widehat{S}_N + F\tau, \tag{3.2}$$

where $\widehat{S}_N(F) = J\widehat{T}_N(F)F^{-T}$ and represents the natural Piola-Kirchhoff response function.

It is known that soft tissue exhibits time-dependent mechanical behavior and should be modeled as viscoelastic material. However, under the effect of the small amplitude, high frequency ultrasound wave superimposed on the arterial inner wall,

the glassy material property of the tissue is dominant, so it is reasonable to model the arteries as a nonlinear elastic material. This equals to specifying a strain-energy function $\widehat{W}(F)$ for the constitutive model such that

$$\widehat{S}_N(F) = \partial_F \widehat{W}(F), \tag{3.3}$$

and

$$S = \partial_F \widehat{W}(F) + \tau F. \tag{3.4}$$

Many experiments show that intact arteries are layered, anisotropic, slightly compressible, heterogeneous, residually stressed, elastic or viscoelastic material bodies [5, 16, 17, 26]. They also exhibit nonlinear stress-strain behavior. To incorporate some of the properties, we adopt the slightly compressible neo-Hookean model for the strain energy function as the natural response of the material [15] given by

$$\widehat{W}(F) := \mu\Big(\phi(J) + \frac{1}{2}(|F|^2 - 3)\Big), \tag{3.5}$$

where $J = \det(F)$, $\phi(x) = \frac{1}{2\beta}(x^{-2\beta} - 1)$, $\beta = \frac{\nu}{1-2\nu}$, μ is shear modulus and ν is Poisson's ratio.

3.3 Construction of Boundary Value Problems

The unloaded, residually stressed reference configuration of arterial wall is idealized as an infinitely long axisymmetric cylindrical tube. The radius of cross-sectional wall satisfies $R_I \leq R \leq R_O$, where R_I and R_O express the inner wall radius and the outer wall radius respectively.

The cylindrical curvilinear basis (j_1, j_2, j_3) is used for this specified geometrical

model, the form of which is

$$j_1 = \cos(\Theta)e_1 + \sin(\Theta)e_2, \quad j_2 = -\sin(\Theta)e_1 + \cos(\Theta)e_2, \quad j_3 = e_3, \tag{3.6}$$

where (e_1, e_2, e_3) is the natural Euclidean orthonormal basis. The three variables (R, Θ, Z) represent the radius, angle for cross section and axial length respectively in cylindrical basis.

As the IVUS is interrogating inside the artery, its wave frequency of sound is in the MHz range. Additionally, the artery is naturally subjected to a pulsatile, time-dependent loading of roughly 1 Hz frequency. So compared with the MHz range, the deformation caused by frequency of 1 Hz can be idealized as being quasistatic. Under such simplification, two categories of deformations are speculated. One is the quasistatic deformations of the vessel wall caused by constant blood pressure denoted by π . The other one is the small amplitude, high frequency vibrations superimposed on the quasistatic deformation from IVUS interrogation. This two categories of deformations generates two kinds of boundary value problems.

3.3.1 Quasistatic Deformation Problem

Under the unloaded residually stressed reference configuration, the inner wall subjected to blood pressures produces a class of axisymmetric deformations of the form

$$\chi_0 = r_0(R)j_1(\Theta) + \lambda_0(R)Zj_3, \tag{3.7}$$

where $r_0(R)$ and $\lambda_0(R)$ represent the radial stretch and axial stretch respectively. $\lambda_0(R)$ is assumed to be 1 in this dissertation.

The outer boundary β_O is assumed to be stress free and the inner boundary β_I is assumed to be subjected only to constant blood pressures. Thus, by the equations

of motion (2.5), the first category of boundary value problems for the quasistatic deformations in the reference configuration is as follows

$$\mathrm{Div} S_0 = 0 \quad \text{in } \beta, \tag{3.8}$$

$$S_0(-j_1) = 0 \quad \text{on } \beta_O, \tag{3.9}$$

$$S_0 j_1 = -\pi J_0 F_0^{-T} j_1 \quad \text{on } \beta_I, \tag{3.10}$$

where F_0 is the deformation gradient of χ_0 expressed as

$$F_0 = r_0' j_1 \otimes j_1 + (\frac{r_0}{R}) j_2 \otimes j_2 + j_3 \otimes j_3, \tag{3.11}$$

$J_0 = \det(F_0)$ and π is the blood pressure in a cardiac cycle.

By (3.2), the boundary conditions (3.9) and (3.10) are rewritten as

$$S_0 j_1 = (\widehat{S}_{0N}(F_0) + \tau F_0) j_1 = \widehat{S}_{0N}(F_0) j_1 + \tau F_0 j_1. \tag{3.12}$$

On the two boundaries, τ arises from the growth and remodeling processes of the biological tissues itself without any external effects, and satisfies the governing equation

$$\begin{aligned} &\mathrm{Div}\tau = 0 \quad \text{on } \beta, \\ &\tau m = 0 \quad \text{on } \partial\beta_O \cup \partial\beta_I, \end{aligned} \tag{3.13}$$

where m denotes the outward unit normal to the inner or outer boundaries of the reference configuration β. Thus, boundary conditions in (3.13) equals $\tau j_1 = 0$. This simplifies (3.12) to be

$$S_0 j_1 = \widehat{S}_{0N}(F_0) j_1. \tag{3.14}$$

(3.9) and (3.10) hence become

$$\widehat{S}_{0N}(F_0)j_1 = 0 \qquad \text{on } \beta_O, \tag{3.15a}$$

$$\widehat{S}_{0N}(F_0)j_1 = -\pi J_0 F_0^{-T} j_1 \qquad \text{on } \beta_I. \tag{3.15b}$$

Substituting (3.5), (3.4) and (3.11) into (3.8) and (3.15), one obtains the boundary value problem for $r_0(R)$ as

$$0 = \mu\left[\psi(J_0)\left(\frac{1}{R}(\frac{R}{r_0'})' - \frac{1}{r_0}\right) + J_0\psi'(J_0)R\left(\frac{(r_0/R)'}{(r_0r_0'/R)} - (\frac{1}{r_0'})'\right) + (Rr_0')' - \frac{r_0}{R}\right] + \tau^{22}R(\frac{r_0}{R})' + \tau^{11}Rr_0'' \tag{3.16}$$

$$\psi(J_0) + (r_0')^2 = 0 \qquad \text{for} \qquad R = R_O, \tag{3.17a}$$

$$\mu[\psi(J_0) + (r_0')^2] = -\pi r_0 r_0'/R_I \qquad \text{for} \qquad R = R_I, \tag{3.17b}$$

where $\psi(r_0) = \phi'(r_0)r_0$ and $\phi(r_0)$ is defined in (3.5). Reorganizing (3.16) yields a second order equation

$$r_0'' = \frac{E(R, r_0, r_0')}{F(R, r_0, r_0')}, \tag{3.18}$$

where

$$\begin{aligned} E(R, r_0, r_0') =& \mu r_0^{-2\beta}(r_0')^{-2\beta-1}R^{2\beta-1} - \mu r_0^{-2\beta-1}(r_0')^{-2\beta}R^{2\beta} \\ & - 2\beta\mu(r_0r_0')^{-2\beta-1}(r_0'R - r_0)R^{2\beta} - \mu r_0' + \mu r_0R^{-1} - \tau^{22}(r_0'R - r_0)R^{-1}, \\ F(R, r_0, r_0') =& \mu(1 + 2\beta R)r_0^{-2\beta}(r_0')^{-2\beta-2}R^{2\beta} + \mu R + \tau^{11}R. \end{aligned} \tag{3.19}$$

The boundary conditions in (3.17) also become

$$-(\frac{r_0 r_0'}{R})^{-2\beta} + (r_0')^2 = 0 \qquad \text{for} \qquad R = R_O, \tag{3.20a}$$

$$\mu[-(\frac{r_0 r_0'}{R})^{-2\beta} + (r_0')^2] = -\pi r_0 r_0'/R_I \qquad \text{for} \qquad R = R_I. \tag{3.20b}$$

3.3.2 Small Amplitude High Frequency Vibrational Deformation

Under the IVUS implementation, the inner wall is subjected to two pressures: the pulsatile blood pressure and the pressure from the small amplitude, high frequency ultrasound wave. This two can be combined to form a time harmonic blood pressure as

$$\pi_t = \pi(1 + \varepsilon e^{i\omega t}), \tag{3.21}$$

where ε is an infinitesimally small quantity, ω is the frequency of IVUS wave and i is the imaginary unit of complex number satisfying $i^2 = -1$. Performing an asymptotic expansion, we obtain the following forms

$$r(R,t) = r_0(R) + \varepsilon r_1(R)e^{i\omega t} + o(\varepsilon) \tag{3.22a}$$

$$u(X,t) = u_0(X) + \varepsilon u_1(X)e^{i\omega t} + o(\varepsilon) \tag{3.22b}$$

$$F(X,t) = I + \bigtriangledown u(X,t) = F_0(X) + \varepsilon \bigtriangledown u_1(X)e^{i\omega t} + o(\varepsilon) \tag{3.22c}$$

$$S(X,t) = S_0(X) + \varepsilon S_1(X)e^{i\omega t} + o(\varepsilon) \tag{3.22d}$$

$$\lambda(X,t) = \lambda_0(X) + \varepsilon \lambda_1(X)e^{i\omega t} + o(\varepsilon) \tag{3.22e}$$

where X, $u(X,t)$ and $\lambda(X,t)$ express the three dimensional position vector, displacement and the axial stretch factor respetively, quantities subscripted with 0 correspond to the static deformation, and quantities subscripted with 1 correspond to the first-order perturbational terms.

The boundary value problem governing the linearized free vibrations for pure radial resonant frequencies (as $\lambda_1 = 0$) is [27]

$$\begin{aligned}
-\omega^2 r_1 =& \mu\Big[r_1'' + (\frac{r_1}{R})' - 2\beta J_0^{-2\beta}\Big(\frac{r_0''}{r_0'} + \frac{(r_0/R)'}{(r_0/R)}\Big)\Big(2\beta\frac{1}{r_0'}(\frac{r_1'}{r_0'} + \frac{r_1}{r_0}) + \frac{r_1'}{(r_0')^2}\Big) \\
&+ J_0^{-2\beta}\big[2\beta\big[\frac{1}{r_0'}(\frac{r_1'}{r_0'} + \frac{r_1}{r_0})' + (\frac{r_1'}{r_0'} + \frac{r_1}{r_0})(\frac{1}{R}(\frac{R}{r_0'})' - \frac{1}{r_0})\big] \\
&+ \frac{1}{R}(\frac{Rr_1'}{(r_0')^2})' - \frac{r_1}{r_0^2} - (\frac{\lambda_0'}{\lambda_0 r_0'})(\frac{r_1'}{r_0'})\big]\Big] \\
&+ \tau^{22}(\frac{r_1}{R})' + \tau^{11}r_1'',
\end{aligned} \tag{3.23}$$

with inner and outer homogeneous boundary conditions

$$\frac{2\beta}{r_0'}(\frac{r_1'}{r_0'} + \frac{r_1}{r_0}) + \frac{r_1'}{(r_0')^2} + J_0^{2\beta}r_1' = 0, \qquad R = R_I, R_O, \tag{3.24}$$

where r_0 is solution of (3.16) and (3.17).

Reorganizing (3.23) to be a second order homogeneous differential equation gives

$$F(R)r_1'' + Q(R)r_1' + G(R)r_1 = \lambda E(R)r_1, \tag{3.25}$$

where

$$F(R) = 1 + \frac{J_0^{-2\beta}2\beta}{(r_0')^2} + \frac{J_0^{-2\beta}}{(r_0')^2} + \frac{\tau^{11}}{\mu}, \tag{3.26}$$

$$\begin{aligned}
Q(R) = \frac{1}{R} - 2\beta J_0^{-2\beta}\Big[\ln(|\frac{r_0 r_0'}{R}|)\Big]'\Big[\frac{2\beta+1}{(r_0')^2}\Big] + 2\beta J_0^{-2\beta}\Big[\frac{1}{r_0'}(\frac{1}{r_0'})' + \frac{1}{Rr_0'}(\frac{R}{r_0'})'\Big] \\
+ J_0^{-2\beta}\frac{1}{R}(\frac{R}{(r_0')^2})' + \frac{\tau^{22}}{\mu R},
\end{aligned} \tag{3.27}$$

$$G(R) = -\frac{1}{R^2} - \frac{(2\beta)^2 J_0^{-2\beta}}{r_0 r_0'}\Big[\ln(|\frac{r_0 r_0'}{R}|)\Big]' + 2\beta J_0^{-2\beta}\Big[\frac{1}{r_0'}(\frac{1}{r_0})' + \frac{1}{Rr_0}(\frac{R}{r_0'})' - \frac{1}{r_0^2}\Big] - J_0^{-2\beta}\frac{1}{r_0^2} - \frac{\tau^{22}}{R^2\mu}, \quad (3.28)$$

$$E(R) = -1, \quad (3.29)$$

and $\lambda = \omega^2/\mu$.

(3.25) yields a SLP

$$-\frac{d}{dR}(p(R)\frac{dr_1(R)}{dR}) + q(R)r_1(R) = \lambda W(R)r_1(R), \quad (3.30)$$

where

$$p(R) = e^{\int (Q/F)dR}, \quad (3.31a)$$

$$q(R) = -\frac{G}{F}e^{\int (Q/F)dR}, \quad (3.31b)$$

$$W(R) = \frac{e^{\int (Q/F)dR}}{F}. \quad (3.31c)$$

Boundary conditions (3.24) can be rearranged to be

$$\Big(\frac{2\beta}{(r_0')^2} + \frac{1}{(r_0')^2} + J_0^{2\beta}\Big)r_1' + \frac{2\beta}{r_0 r_0'}r_1 = 0, \qquad R = R_I, R_O. \quad (3.32)$$

4. CONSTRUCTION OF ALGORITHMS AND NUMERICAL EXAMPLES*

In this chapter, we will devise algorithms for recovering the shear modulus μ and τ^{11} of the residual stress tensor. As we recover the shear modulus, residual stress is ignored in the modeling. As we recover τ^{11} or τ^{22}, μ is fixed to be 27 kPa and other components of the residual stress tensor are set to be zero.

4.1 The Cubic Spline Interpolation

The IVUS technique only obtains the first several lower-mode eigenfrequencies of the vessel wall for each blood pressure accurately. An approximation of the unknown function $g(R)$ ($g(R) = \mu(R)$ for shear modulus and $g(R) = \tau^{11}(R)$ for residual stress) is herein recovered by this limited information. The cubic spline interpolation is mainly utilized for such approximation. The domain $[R_I, R_O]$ is uniformly partitioned into $N-1$ subintervals, where the nodes are denoted as R_1, $R_2, \ldots R_N$. The value of $g(R)$ at R_i is denoted by g_i for $1 \leq i \leq N$. The N points (R_i, g_i) are interpolated by cubic splines to be

$$g(R) = P_i(R), \quad \text{for} \quad R_i \leq R \leq R_{i+1}, \tag{4.1}$$

for $1 \leq i \leq N-1$, where each $P_i(R)$ is a cubic polynomial satisfying

$$\text{continuity:} \quad P_i(R_i) = g_i, \quad P_i(R_{i+1}) = g_{i+1}, \tag{4.2}$$

$$\text{first-order differentiability:} \quad P_i'(R_{i+1}) = P_{i+1}'(R_i). \tag{4.3}$$

*Part of the chapter is reprinted with permission from "Recovery of the shear modulus of hyperelastic soft tissue by an inverse spectral technique" by Kun Gou, Sunnie Joshi, Jay Walton, 2012. International Journal of Engineering Science, 56, 1-16, Copyright [2012] by Elsevier B.V.

A sample function of 4-node interpolation is given in Figure 4.1, where $[R_I, R_O]$ is partitioned into 3 equal subintervals, and the 4 points for interpolation are $(3.302, 0.5)$, $(3.5363, 1.2)$, $(3.7707, 0.8)$ and $(4.005, 1.6)$.

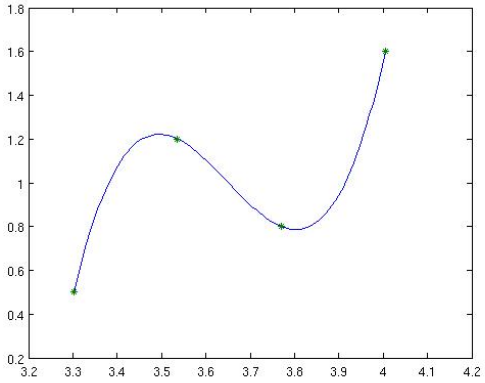

Figure 4.1: A sample of piecewise cubic spline function with 4 given nodes.

Consequently, recovering $g(R)$ amounts to estimating g_i for $1 \leq i \leq N$ and the approximated function is given by (4.1) from the interpolation. For an abuse of notation, the following identity is utilized

$$g(R) = (g_1, g_2, g_3, \cdots g_N). \tag{4.4}$$

Except the cubic spline interpolation, one can also apply its piecewise form which discards the first-order differentiability at the nodes. The derivatives of the interpolation at the first and last nodes can also be customarily prescribed. In Matlab, the default derivatives at the two end nodes are set to be zero.

From (3.18) and (3.20) and (3.30-3.32), we know the following results:

1. r_0 is a function of $g(R)$ and π, i.e. $r_0(R) = r_0\Big(\pi, g(R), R\Big)$ and can only be evaluated numerically;

2. $p(R)$, $q(R)$, $W(R)$ in (3.31) and coefficients for r_1 and r_1' in the boundary

conditions (3.32) are all functions of r_0. Thus they are also functions of $g(R)$ and π.

An algorithm for solving this kind of inverse spectral problem is developed in the next sections.

4.2 Algorithms for Recovering the Shear Modulus

4.2.1 Some Basic Algorithms

Some basic algorithms are needed, including the generalized secant method for finding root of a system of nonlinear equations, the fourth-order Runge Kutta method for finding solution of an initial value problem, the shooting method for finding solution of a boundary value problem and the Sleign2 method for finding eigenvalues of SLP. The details of the last three methods are discussed in the appendix. The generalized secant method is explained in this section.

One dimensional secant method works to find the solution of an equation $f(t) = 0$. The iterative formula is

$$t_k = t_{k-1} - \frac{t_{k-2} - t_{k-1}}{f(t_{k-2}) - f(t_{k-1})} f(t_{k-1}). \tag{4.5}$$

It stops if for some tolerance number ε, $|f(t_k)| < \varepsilon$ or $|f(t_k) - f(t_{k-1})| < \varepsilon$. We need two initial guesses t_0 and t_1 near the root for the method.

Meanwhile, multidimensional secant method works to find the root of n linear or

nonlinear equations with n unknowns

$$\begin{aligned} f_1(x_1,x_2,.....x_n) &= 0, \\ f_2(x_1,x_2,.....x_n) &= 0, \\ &..... \\ f_n(x_1,x_2,.....x_n) &= 0. \end{aligned} \tag{4.6}$$

Similar to the one dimensional secant method, we need $n+1$ trial solutions to start the method and denote them by the following identities

$$\begin{aligned} X_1 &= (x_1^{(1)}, x_2^{(1)}, ...x_n^{(1)}), \\ X_2 &= (x_1^{(2)}, x_2^{2)}, ...x_n^{(2)}), \\ &..... \\ X_{n+1} &= (x_1^{(n+1)}, x_2^{(n+1)}, ...x_n^{(n+1)}). \end{aligned} \tag{4.7}$$

Set $n+1$ numbers Π_1, Π_2,...Π_{n+1} to satisfy the following $n+1$ equations

$$\begin{aligned} &\sum_{j=1}^{n+1} \Pi_j = 1, \\ &\sum_{j=1}^{n+1} \Pi_j f_i(x_1^{(j)}, x_2^{(j)}, ...x_n^{(j)}) = 0 \quad \text{for} \quad i = 1, 2, ...n. \end{aligned} \tag{4.8}$$

Solve for Π_1, Π_2,...Π_{n+1} from (4.8) and form a new vector

$$X^* = \sum_{j=1}^{n+1} \Pi_j X^{(j)}. \tag{4.9}$$

Compare the $n+1$ values

$$s_j = \sum_{i=1}^{n} |f_i(x_1^{(j)}, x_2^{(j)}, ...x_n^{(j)})|^{\Omega} \quad \text{for} \quad j = 1, 2, ...n+1, \tag{4.10}$$

where Ω is set according to different problems and usually it can be 1, 2, 3, 4. Let

$$s_\kappa = \max_{1 \le j \le n+1} s_j.$$

We thus obtain a number κ. In (4.7), replace X_κ by X^*. Another new set of trial solutions (4.7) is thus formed. We repeat the above process until we find a satisfactory solution. The stopping criteria can be established to be

$$|X^*_{new} - X^*_{old}| < \varepsilon_1,$$

where ε_1 is the tolerance number, X^*_{new} is the updated X^*, and X^*_{old} means the X^* from last iteration. Local convergence of the method is shown in [24]. We notice that as $n = 1$ it reduces to the one dimensional secant method.

4.2.2 Shooting Method for Inverse Sturm-Liouville Problem

Though complicated, the advantage of this inverse problem is that we know the exact function formulas of the coefficients of SLP in (3.30). We can make use of this information to design a new algorithm called the *Shooting Method for Inverse Sturm-Liouville Problem.*

To recover N unknowns in $\mu = (\mu_1, \mu_2, ...\mu_N)$, we need N equations. We make use of N different blood pressures π_1, π_2,...π_N to reach this aim. For each π_j, we can acquire a sequence of eigenfrequencies from experiments and denote them as $\{\lambda_n^{(j)}\}_{n=1}^{\infty}$. For each π_j and an initial guess $\mu = (\mu_1, \mu_2, ...\mu_N)$ from which we know

the corresponding cubic spline function $\mu(R)$, we find the solution $r_0(\mu, R)$ from (3.18) and (3.20). Then substitute $r_0(\mu, R)$, $\mu(R)$ and blood pressure π_j into (3.30) and (3.32) to find the sequence of eigenvalues depending on μ and π_j as $\{\lambda_n^{(j)}(\mu)\}_{n=0}^{\infty}$. We define the distance† between$\{\lambda_n^{(j)}\}_{n=0}^{\infty}$ and $\{\lambda_n^{(j)}(\mu)\}_{n=0}^{\infty}$ as

$$d_j(\mu) = \sum_{n=0}^{\infty} |\lambda_n^{(j)}(\mu) - \lambda_n^{(j)}|^{\Gamma}, \tag{4.11}$$

where Γ is a parameter we will specify case by case. We then find the μ such that $d_j(\mu) \approx 0$ for j=1, 2,...N (notice that $d_j(\mu) = 0$ can not be reached since μ is only an approximation of the real shear modulus). We apply the secant method described in Section 4.2.1 to solve these equations.

We remark that we can not get infinitely many eigenfrequencies λ_j from experiments. However, the first few eigenfrequencies, say the first five or less, are enough to recover an accurate μ, so a practical and effective substitute for (4.11) is

$$d_j(\mu) = |\lambda_0^{(j)}(\mu) - \lambda_0^{(j)}|^{\Gamma}. \tag{4.12}$$

The detailed algorithm is as follows:

1. Give a tolerance number ε_1, say 10^{-4} for the generalized secant method and another tolerance number ε_2, say 10^{-13} for other iterative parts;

2. Guess $N+1$ values $\mu^{(1)}$, $\mu^{(2)}$,...$\mu^{(N+1)}$ for μ (each value is a vector with N components and represents a cubic spline function). Make sure these guesses are near the educated estimate of real μ so that the algorithm is locally convergent;

3. For each $\mu^{(i)}$ in Step 2 (for the first iteration) or Step 9 (for later iterations), and each blood pressure π_j, where $1 \leq j \leq N$, we find the numerical solu-

†This is not a distance in a mathematically strict sense.

tion $r_0^{(j)}(R, \mu^{(i)})$ from (3.18) and (3.20) respectively. The secant method and shooting methods are used for solving the boundary value problems;

4. Plugging $r_0^{(j)}(R, \mu^{(i)})$, $\mu^{(i)}$ and π_j into the Equations (3.30-3.32) and by Sleign2 method we can find the first eigenvalue for the SLP (3.30) which are denoted as $\lambda_0^{(j)}(\mu^{(i)})$;

5. Plug $\lambda_0^{(j)}(\mu^{(i)})$ into Equation (4.12) and get $d_j(\mu^{(i)})$;

6. Set a $(N+1) \times (N+1)$ square matrix A by

$$\mathbf{A} = \begin{bmatrix} d_1(\mu^{(1)}) & d_1(\mu^{(2)}) & \dots & d_1(\mu^{(N+1)}) \\ d_2(\mu^{(1)}) & d_2(\mu^{(2)}) & \dots & d_2(\mu^{(N+1)}) \\ \vdots & \vdots & \vdots & \vdots \\ d_N(\mu^{(1)}) & d_N(\mu^{(2)}) & \dots & d_N(\mu^{(N+1)}) \\ 1 & 1 & \dots & 1 \end{bmatrix}; \tag{4.13}$$

7. Find the vector $\Pi = (\Pi_1, \Pi_2, ...\Pi_{(N+1)})$ from the matrix equation $A\Pi^T = (0, 0, 0, ...0, 1)^T$, where the superscript T stands for transpose;

8. By Equation (4.9) in Section 4.2.1, we find an updated μ^*;

9. Compute s_i for $1 \leq i \leq N+1$ from the method in Section 4.2.1 and find the value κ such that s_κ is the biggest among all these values. Then replace $\mu^{(\kappa)}$ by μ^* and form an updated $N+1$ values $\mu^{(1)}$, $\mu^{(2)}$,...$\mu^{(\kappa-1)}$, μ^*, $\mu^{(\kappa+1)}$...$\mu^{(N+1)}$ for μ;

10. If $|\mu^*_{new} - \mu^*_{old}| < \varepsilon_1$ (μ^*_{new} is the current updated μ^* and μ^*_{old} is the updated μ^* from last iteration), stop and μ^*_{new} is the value we want. If not, go to Step 3.

4.2.3 Numerical Examples

For the three examples below, we set that $\beta = 2$, i.e. $\nu \approx 0.4$, the radius of inner boundary $R_I = 3.302$ mm and the radius of outer boundary $R_O = 4.005$ mm. In each table, the first row represents the blood pressures used for that example. The second row represents the related first eigenmode of that pressure. Each table contains a number of sets of initial guesses for μ at nodes $R_1, R_2, ...R_N$ for the multidimensional secant method. For the output, we have the returned value of μ at each node, the iterational number of that input and relative errors computed in norm of L^1, L^2 and L^∞ respectively. In the figures, solid curves represent the original function plots and dashed curves mean the approximations.

pressure($mmHg$)	100	120	140
frequency($\times 10^6 Hz$)	3.8128	4.3736	4.8624
parameter	$\Gamma = 5$		$\Omega = 2$
initial guess 1 (kPa)	1.3	0.87	0.48
initial guess 2 (kPa)	0.98	0.93	0.57
initial guess 3 (kPa)	0.95	0.89	0.46
initial guess 4 (kPa)	1.15	0.88	0.55
returned value (kPa)	0.9777	0.8933	0.4837
iteration number	5		
relative error	L^1	L^2	L^∞
	0.0130	0.0146	0.0223

Table 4.1: Numerical input and output of Example 4.2.1 with 3 nodes

pressure($mmHg$)	100	110	120	130	140
frequency($\times 10^6 Hz$)	3.8128	4.1045	4.3736	4.6249	4.8624
parameter	$\Gamma = 4$			$\Omega = 3$	
initial guess 1 (kPa)	1.3	0.925	0.87	0.7	0.52
initial guess 2 (kPa)	0.98	0.88	0.93	0.75	0.57
initial guess 3 (kPa)	0.95	0.93	0.89	0.68	0.525
initial guess 4 (kPa)	1.15	0.91	0.88	0.73	0.55
initial guess 5 (kPa)	1.05	0.95	0.85	0.72	0.51
initial guess 6 (kPa)	0.955	0.92	0.875	0.71	0.49
returned value (kPa)	0.9797	0.9389	0.8549	0.7051	0.4798
iteration number	11				
relative error	L^1		L^2		L^∞
	0.0277		0.0279		0.0305

Table 4.2: Numerical input and output of Example 4.2.1 with 5 nodes

pressure($mmHg$)	110	120	130	140	150
frequency($\times 10^6 Hz$)	6.2032	6.6059	6.9824	7.3386	7.6798
parameter	$\Gamma = 4$			$\Omega = 3$	
initial guess 1 (kPa)	1	1.7	2.0	1.7	0.9
initial guess 2 (kPa)	1.1	1.6	1.9	1.6	0.8
initial guess 3 (kPa)	0.9	1.8	2.1	1.8	1.1
initial guess 4 (kPa)	1.2	1.6	1.95	1.6	1.2
initial guess 5 (kPa)	0.8	1.75	2.05	1.75	0.95
initial guess 6 (kPa)	0.9555	1.65	1.9555	1.7555	1.1555
returned value (kPa)	0.9844	1.6895	1.9913	1.7193	0.9792
iteration number	13				
relative error	L^1		L^2		L^∞
	0.0070		0.0077		0.0104

Table 4.4: Numerical input and output of Example 4.2.2 with 5 nodes

pressure($mmHg$)	110	130	140
frequency($\times 10^6 Hz$)	6.2032	6.9824	7.3386
parameter	$\Gamma = 2$		$\Omega = 5$
initial guess 1 (kPa)	1	1.85	1.15
initial guess 2 (kPa)	0.9	2.05	0.85
initial guess 3 (kPa)	0.85	1.95	0.9
initial guess 4 (kPa)	1.1	2	1.1
returned value (kPa)	0.9897	1.8462	1.1434
iteration number	13		
relative error	L^1	L^2	L^∞
	0.0542	0.0614	0.0785

Table 4.3: Numerical input and output of Example 4.2.2 with 3 nodes

Example 4.2.1 The original function is $\mu = -(R - R_I)^2 + 1$, decreasing through the domain. We use cubic spline interpolation with 3 nodes and 5 nodes respectively

pressure($mmHg$)	90	100	110	120	130	140	150
frequency($\times 10^6 Hz$)	5.2878	5.7668	6.2032	6.6059	6.9824	7.3386	7.6798
parameter	$\Gamma = 2$					$\Omega = 2$	
initial guess 1 (kPa)	1	1.45	1.7	2.0	1.7	1.4	0.9
initial guess 2 (kPa)	1.1	1.4	1.65	1.9	1.65	1.3	0.8
initial guess 3 (kPa)	0.9	1.5	1.8	2.1	1.7	1.4	1.1
initial guess 4 (kPa)	1.15	1.455	1.655	1.95	1.6	1.35	1.15
initial guess 5 (kPa)	0.85	1.35	1.75	2.05	1.8	1.5	0.95
initial guess 6 (kPa)	0.955	1.5	1.85	1.955	1.755	1.5	1.155
initial guess 7 (kPa)	1.05	1.355	1.75	2.1	1.8	1.4	0.85
initial guess 8 (kPa)	1.15	1.65	1.82	2.15	1.75	1.68	1.05
returned value (kPa)	1.0104	1.4299	1.7541	2.0423	1.7534	1.4308	0.9428
iteration number	6						
relative error	L^1		L^2			L^∞	
	0.0384		0.0453			0.0644	

Table 4.5: Numerical input and output of Example 4.2.2 with 7 nodes

pressure($mmHg$)	110	120	130	140	150
frequency($\times 10^6 Hz$)	3.3242	3.6057	3.8686	4.1148	4.3459
parameter	$\Gamma = 4$			$\Omega = 3$	
initial guess 1 (kPa)	1.4	2.45	1.5	0.4	1.5
initial guess 2 (kPa)	1.45	2.4	1.6	0.45	1.62
initial guess 3 (kPa)	1.5	2.55	1.49	0.53	1.58
initial guess 4 (kPa)	1.63	2.62	1.47	0.58	1.49
initial guess 5 (kPa)	1.57	2.58	1.46	0.48	1.45
initial guess 6 (kPa)	1.62	2.47	1.56	0.56	1.56
returned value (kPa)	1.4933	2.5148	1.4915	0.5307	1.5909
iteration number	31				
relative error	L^1		L^2		L^∞
	0.0504		0.0543		0.0786

Table 4.6: Numerical input and output of Example 4.2.3 with 5 nodes

pressure($mmHg$)	90	100	110	120	130	140	150
frequency($\times 10^6 Hz$)	2.6815	3.0198	3.3242	3.6057	3.8686	4.1148	4.3459
parameter	$\Gamma = 4$					$\Omega = 3$	
initial guess 1 (kPa)	1.4	2.2	2.3	1.5	0.7	0.8	1.5
initial guess 2 (kPa)	1.45	2.25	2.32	1.6	0.75	0.78	1.62
initial guess 3 (kPa)	1.5	2.3	2.35	1.49	0.78	0.75	1.58
initial guess 4 (kPa)	1.63	2.18	2.37	1.47	0.66	0.62	1.49
initial guess 5 (kPa)	1.57	2.27	2.29	1.46	0.65	0.68	1.45
initial guess 6 (kPa)	1.62	2.35	2.26	1.56	0.82	0.65	1.56
initial guess 7 (kPa)	1.42	2.22	2.27	1.46	0.77	0.81	1.48
initial guess 8 (kPa)	1.62	2.19	2.23	1.61	0.73	0.81	1.60
returned value (kPa)	1.5019	2.3325	2.2398	1.5712	0.5758	0.6841	1.4692
iteration number	22						
relative error	L^1		L^2			L^∞	
	0.0369		0.0399			0.0573	

Table 4.7: Numerical input and output of Example 4.2.3 with 7 nodes

to approximate this function. See Tables 4.1 and 4.2 for the input and output data, and Fig. 4.2 for plots of the original function and its approximations.

Example 4.2.2 The original function is $\mu = \sin(\pi(R - R_I)/L) + 1$ with one peak in its plot. We use interpolation with 3 nodes, 5 nodes and 7 nodes respectively to approximate it. See Tables 4.3, 4.4 and 4.5 for the input and output data, and Fig. 4.3 and 4.4 for plots.

Example 4.2.3 The last one is more complicated with one upward peak and one downward peak in its plot. The function formula is $\mu = \sin(2\pi(R - R_I)/L) + 1.5$. 5 node and 7 node interpolations are used respectively for approximation. See Tables 4.6 and 4.7 for data input and output, and Fig. 4.5 for plots.

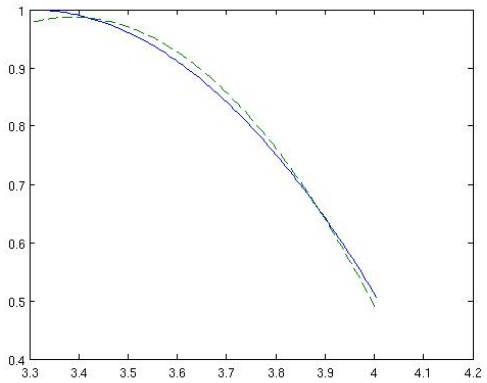

(a) Approximation with 3 nodes.

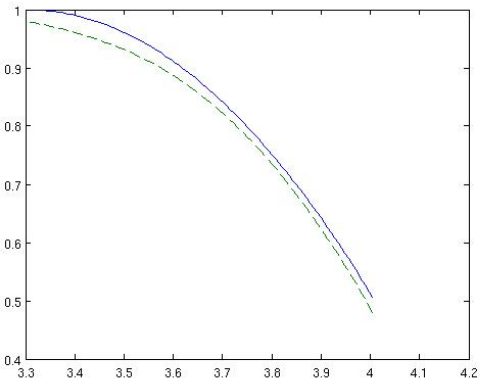

(b) Approximation with 5 nodes.

Figure 4.2: Approximation for Example 4.2.1.

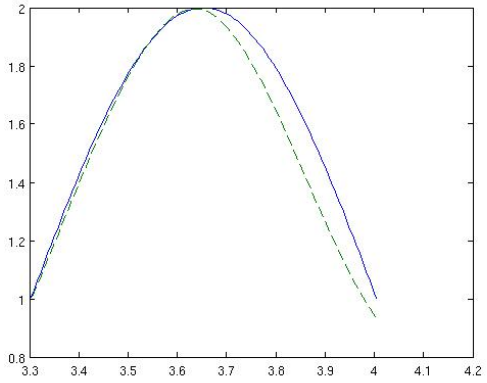

(a) Approximation with 3 nodes.

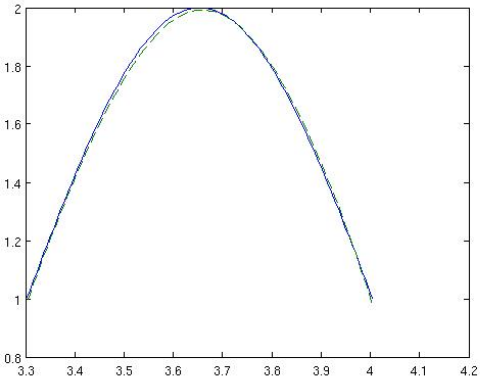

(b) Approximation with 5 nodes.

Figure 4.3: Approximation for Example 4.2.2.

Next, we provide some analysis for the data used and the results obtained.

Preconditioning for SLP: As we can see from these tables, the values of frequency ω from IVUS implementation are in the order of 10^6. The actual eigenvalues λ we compute from (3.30) by Sleign2 method are in the order of square of ω, i.e.,

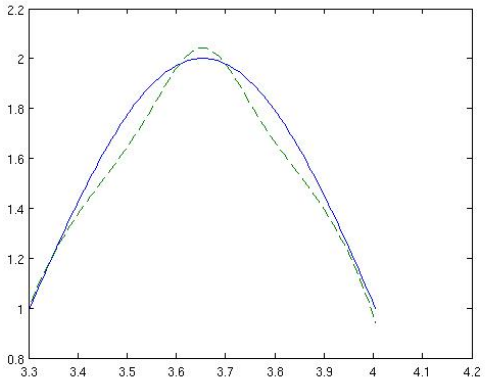

Figure 4.4: Approximation with 7 nodes for Example 4.2.2.

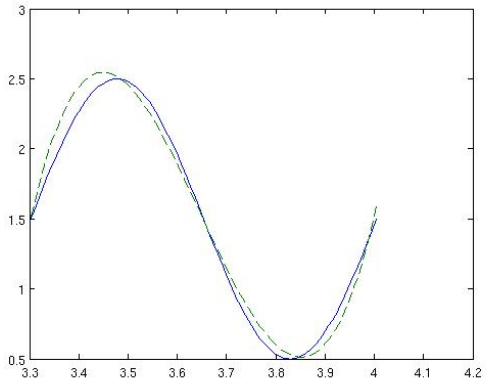

(a) Approximation with 5 nodes.

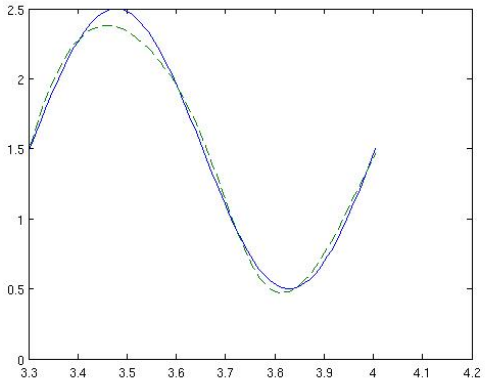

(b) Approximation with 7 nodes.

Figure 4.5: Approximation for Example 4.2.3.

10^{12}. These are large numbers for the computer to manipulate. Operationally, more huge numbers will emerge driving the memory to go out of its scope easily. To avoid such complications, we design a preconditioner for the algorithm. We multiply both sides of (3.30) by ε, a quantity close to zero. The new eigenvalue, $\lambda\varepsilon$, is a number much smaller than the actual one, and hence, it is easier for the machine to execute. The authors tried a few possible ε and found 10^{-12} to be the most suitable one. Too high or too low ε fails to work more effectively.

Errors: For the generalized secant method, we only have local convergence and hence, more scattered guessed data might cause large error. In Example 4.2.1, the relative errors from approximation with 3 nodes are even smaller than that with 5 nodes, because more nodes and guesses may make the data more scattered away from the real ones. This suggests that a symmetric distribution of initial guesses around the real value is an important factor influencing the accuracy. Therefore, one needs to make an educated estimation of the real value for each node, and distribute the initial guesses for the same node inside a small interval around that estimation nearly symmetrically. If possible, small number of nodes is preferred for the approximation.

Parameters Γ and Ω: As Γ or Ω increases, values of (4.10) and (4.12), whose bases are less than 1, decrease. Generally, this causes the algorithm to converge with less iterations. Thus, in most cases, it is true that larger values of Γ and Ω make the algorithm more accurate. However, if Γ and Ω are too large, the matrix (4.13) appearing in the algorithm becomes badly scaled, and this results in poor convergence. Thus, different values for Γ and Ω were tested for each of the examples, and the most suitable ones were chosen based on both accuracy and convergence.

Number of nodes N: The number of nodes N depends on the function we are trying to approximate. For instance, in Example 4.2.3, we use 5 and 7 nodes for approximating $\mu = \sin(2\pi(R - R_I)/L) + 1.5$. Approximation with 3 nodes does not

guarantee convergence for this function. Instead, cubic splines with 5 and 7 nodes can better reflect the curve shape, and thus give better approximations. Therefore, one needs to have an estimation of the shape of the function to select a reasonable N. This information is usually not available beforehand, so one should try several N's to see which one actually converges, and choose the one that gives the best result.

4.3 Reconstruction of Residual Stress

4.3.1 Formulation of Inverse Spectral Problem

The SLP (3.30) depends on the value of the blood pressure π. To indicate such dependence, $p(R)$, $q(R)$ and $W(R)$ are redenoted by $p_{\pi_i}(R)$, $q_{\pi_i}(R)$ and $W_{\pi_i}(R)$, where i is a subscript to indicate variation of blood pressures. The same change is also applied to r_1 and the boundary conditions. Under the new notation, (3.30) and (3.32) develop into

$$-\frac{d}{dR}(p_{\pi_i}(R)\frac{dr_{1\pi_i}(R)}{dR}) + q_{\pi_i}(x)r_{1\pi_i}(R) = \lambda W_{\pi_i}(R)r_{1\pi_i}(R), \tag{4.14}$$

$$\begin{aligned} a_{0\pi_i}r_{1\pi_i}(R) + a_{1\pi_i}r_{1\pi_i}'(R) = 0 \quad \text{for} \quad R = R_I, \\ b_{0\pi_i}r_{1\pi_i}(R) + b_{1\pi_i}r_{1\pi_i}'(R) = 0 \quad \text{for} \quad R = R_O, \end{aligned} \tag{4.15}$$

where

$$a_{0\pi_i} = C_1(R_I), \quad a_{1\pi_i} = C_2(R_I), \tag{4.16}$$

$$b_{0\pi_i} = C_1(R_O), \quad b_{1\pi_i} = C_2(R_O), \tag{4.17}$$

with $C_1(R)$ and $C_2(R)$ denoting the coefficients of r_1' and r_1 in (3.32) respectively, i.e.

$$C_1(R) = \frac{2\beta}{(r_0')^2} + \frac{1}{(r_0')^2} + J_0^{2\beta} \tag{4.18}$$

$$C_2(R) = \frac{2\beta}{r_0 r_0'}. \tag{4.19}$$

The so called *prüfer transformation* is used in Sleign2 algorithm for computing eigenvalues of SLP [45]. It transforms the second-order SLP to a system of equivalent first-order nonlinear system with two dependent variables called the prüfer amplitude and phase denoted by ρ_{π_i} and θ_{π_i} respectively. The transformation is

$$\begin{aligned} r_{1\pi_i}(R) &= \rho_{\pi_i}(R)\sin(\theta_{\pi_i}(R)), \\ p_{\pi_i}(R) r_{1\pi_i}'(R) &= \rho_{\pi_i}(R)\cos(\theta_{\pi_i}(R)). \end{aligned} \tag{4.20}$$

The system of equations for $\rho_{\pi_i}(R)$ and $\theta_{\pi_i}(R)$ are

$$\theta_{\pi_i}'(R) = \frac{1}{p_{\pi_i}(R)}\cos^2(\theta_{\pi_i}(R)) + (\lambda W_{\pi_i}(R) - q_{\pi_i}(R))\sin^2(\theta_{\pi_i}(R)), \tag{4.21}$$

$$\frac{\rho_{\pi_i}'(R)}{\rho_{\pi_i}(R)} = \frac{1}{2}(\frac{1}{p_{\pi_i}(R)} - \lambda W_{\pi_i}(R) + q_{\pi_i}(R))\sin(2\theta_{\pi_i}(R)), \tag{4.22}$$

where

$$\theta_{\pi_i}(R_I) = -\arctan(\frac{a_{1\pi_i}}{p_{\pi_i}(R_I) a_{0\pi_i}}) \quad \text{for} \quad \theta_{\pi_i}(R_I) \in [0, \pi), \tag{4.23}$$

$$\theta_{\pi_i}(R_O) = -\arctan(\frac{b_{1\pi_i}}{p_{\pi_i}(R_O) b_{0\pi_i}}) + (n+1)\pi \quad \text{for} \quad \theta_{\pi_i}(R_O) - (n+1)\pi \in (0, \pi], \tag{4.24}$$

and $n = 0, 1, 2 \ldots$. In Sleign2 algorithm, the extra boundary condition (4.24) for

$\theta_{\pi_i}(R)$ is used to design a function for computing the eigenvalues. In the inverse spectral technique of this dissertation, it is also utilized for recovering the residual stress.

For each blood pressure π_i, suppose one has eigenvalues λ_j, for $1 \leq j \leq M_{\pi_i}$. An implicit function is defined for τ^{11} and each eigenvalue λ_j from (4.24) by

$$D_{\pi_i}(\tau^{11}, \lambda_j) = \theta^j_{\pi_i}(R_O) + \arctan(\frac{b_{1\pi_i}}{p_{\pi_i}(R_O) b_{0\pi_i}}) - (j+1)\pi \quad \text{for} \quad 1 \leq j \leq M_{\pi_i}, \tag{4.25}$$

where $\theta^j_{\pi_i}(R)$ is the solution of (4.21) and (4.23). If τ^{11} is the real solution, $D_{\pi_i}(\tau^{11}, \lambda_j) = 0$.

Suppose one uses K blood pressures, and for each blood pressure π_i, M_{π_i} eigenvalues are obtained from IVUS implementation[‡] shown below:

$$\text{Blood pressures and their eigenvalues:} \begin{cases} \pi_1: & \lambda_1, \lambda_2, \cdots \lambda_{M_{\pi_1}}; \\ \pi_2: & \lambda_1, \lambda_2, \cdots \lambda_{M_{\pi_2}}; \\ \vdots & \vdots \\ \pi_K: & \lambda_1, \lambda_2, \cdots \lambda_{M_{\pi_K}}. \end{cases} \tag{4.26}$$

Since τ^{11} is represented by N unknowns, at least N equations of the form (4.25) are demanded for calculating the solution to avoid under-determination. Namely, this relation has to be satisfied:

$$\sum_{i=1}^{K} M_{\pi_i} \geq N. \tag{4.27}$$

[‡]For each blood pressure, one may discard a few lower-mode eigenvalues to make them not consecutive in order.

As $\sum_{i=1}^{K} M_{\pi_i} = N$, the system of N equations from (4.25) is denoted by

$$D(\tau^{11}, \Lambda) = 0, \tag{4.28}$$

where τ^{11} is in the form of (4.4) and Λ denotes the set of N eigenvalues.

4.3.2 Analysis for Local Existence and Uniqueness

This section gives proofs for showing local existence and uniqueness of solution for Equations (4.28). For a common use of the notation for independent variable, R is replaced by x (only used in this section). A regular SLP [28] is considered

$$-\frac{d}{dx}(p(x)\frac{du(x)}{dx}) + q(x)u(x) = \lambda W(x)u(x), \tag{4.29}$$

$$\alpha_1 u'(x) + \beta_1 u(x) = 0 \quad \text{for} \quad x = R_I, \tag{4.30}$$

$$\alpha_2 u'(x) + \beta_2 u(x) = 0 \quad \text{for} \quad x = R_O, \tag{4.31}$$

where $p(x)$, $q(x)$ and $W(x)$ are functions of $\tau^{11}(x)$, and $\alpha_1\beta_1 \neq 0$, $\alpha_2\beta_2 \neq 0$.

Lemma 4.3.1 *If λ^* is an eigenvalue of SLP (4.29-4.31), depending on the three coefficients of (4.29), $p(x)$, $q(x)$ and $W(x)$ as a function $\lambda^*(p(x), q(x), W(x))$, and $u(x, \lambda)$ is the solution of the initial value problem*

$$-\frac{d}{dx}(p(x)\frac{du(x)}{dx}) + q(x)u(x) = \lambda W(x)u(x), \tag{4.32}$$

$$\alpha_1 u'(x) + \beta_1 u(x) = 0 \quad \textit{for} \quad x = R_I, \tag{4.33}$$

$$u'(R_I) = 1, \tag{4.34}$$

then the following equation holds

$$\int_{R_I}^{R_O} W(x)u^2(x,\lambda^*)dx = \frac{p(R_O)u'(R_O,\lambda^*)}{\beta_2}\frac{\partial\vartheta(\lambda^*)}{\partial\lambda}, \tag{4.35}$$

where $\vartheta(\lambda) = \alpha_2 u'_\lambda(R_O,\lambda) + \beta_2 u_\lambda(R_O,\lambda)$.

Proof Differentiating (4.29) with respect to λ generates

$$-\frac{d}{dx}(p(x)\frac{du_\lambda(x,\lambda)}{dx}) + q(x)u_\lambda(x,\lambda) = W(x)u(x,\lambda) + \lambda W(x)u_\lambda(x,\lambda). \tag{4.36}$$

Multiplying (4.36) by $u(x,\lambda)$, (4.29) by $u_\lambda(x,\lambda)$ and taking the difference produce

$$\begin{aligned} W(x)u^2(x,\lambda) &= -\Big(p(x)u'_\lambda(x,\lambda)\Big)'u(x,\lambda) + \Big(p(x)u'(x,\lambda)\Big)'u_\lambda(x,\lambda) \\ &= \Big[-p(x)u'_\lambda(x,\lambda)u(x,\lambda) + p(x)u'(x,\lambda)u_\lambda(x,\lambda)\Big]'. \end{aligned} \tag{4.37}$$

Integrating (4.37) with respect to x from R_I to R_O at $\lambda = \lambda^*$ and considering the boundary conditions (4.30) and (4.31) yield

$$\int_{R_I}^{R_O} W(x)u^2(x,\lambda^*)dx = \frac{p(R_O)u'(R_O,\lambda^*)}{\beta_2}\frac{\partial\vartheta(\lambda^*)}{\partial\lambda},$$

where $\vartheta(\lambda) = \alpha_2 u'_\lambda(R_O,\lambda) + \beta_2 u_\lambda(R_O,\lambda)$. ■

Proposition 4.3.1 *$\lambda^*(p(x),q(x),W(x))$ is a real analytic function of $\tau^{11}(x)$ on $L^2[R_I,R_O]$.*

Proof The fact that the SLP (4.29-4.31) is regular means $p(x) > 0$ and $W(x) > 0$ as $x \in [R_O,R_I]$ [28]. $u(x,\lambda^*)$ is the eigenfunction corresponding to the eigenvalue λ^*, so $u(x,\lambda^*)$ is not trivial, i.e. $u(x,\lambda^*) \neq 0$ for some $x \in [R_I,R_O]$. Therefore,

$$\int_{R_I}^{R_O} W(x)u^2(x,\lambda^*)dx > 0. \tag{4.38}$$

(4.35) and (4.38)yield

$$u'(R_O, \lambda^*) \neq 0. \tag{4.39}$$

Since $u'(R_O, \lambda^*)$ are functions of $p(x)$, $q(x)$ and $W(x)$,

$$u'(R_O, \lambda^*) = u'(R_O, p(x), q(x), W(x), \lambda^*) \neq 0. \tag{4.40}$$

The implicit function theorem [47] applies, which implies that there exists a unique real analytic function $\lambda^*(\Phi, \Psi, \Omega)$ defined on some neighborhoods $\Lambda \subset L^2[R_I, R_O]$ of $p(x)$, $\Delta \subset L^2[R_I, R_O]$ of $q(x)$ and $\Upsilon \subset L^2[R_I, R_O]$ of $W(x)$ for Φ, Ψ and Ω respectively such that

$$\lambda^*(p(x), q(x), W(x)) = \lambda^*. \tag{4.41}$$

Nevertheless, $p(x)$, $q(x)$ and $W(x)$ all are analytic functions of $\tau^{11}(x)$, so

$$\lambda^*(p(x), q(x), W(x))$$

is also an analytic function of $\tau^{11}(x)$ and can be denoted by $\lambda^*(\tau^{11})$. ■

Theorem 4.3.2 *(**Existence and Uniqueness**) Provided the Jacobian $\frac{\partial D}{\partial \tau^{11}}$ expressed in (4.43), where D is from Equation (4.28), is nonsingular at $\tau^{11} = 0$ and the given eigenvalue set Λ of (4.26) lies in a sufficiently small neighborhood of the eigenvalue set Λ_0 generated by $\tau^{11} = 0$ through (4.14) and (4.15), then $D = 0$ has a unique solution.*

Proof Λ is in a sufficiently small neighborhood of Λ_0, so by Proposition 4.3.1, there exists sufficiently small $\widetilde{\tau}^{11}$ such that it generates Λ through (4.14) and (4.15) which makes $D = 0$.

Also, by Proposition 4.3.1, λ^* continuously depends on τ^{11} and D continuously

depends on λ^*, so D is continuously dependent on τ^{11}. Consequently, since $\frac{\partial D}{\partial \tau^{11}}$ is nonsingular at $\tau^{11} = 0$ and $\widetilde{\tau}^{11}$ is sufficiently small, $\frac{\partial D}{\partial \tau^{11}}$ is also nonsingular at $\widetilde{\tau}^{11}$. By implicit function theorem applied on $D(\Lambda, \widetilde{\tau}^{11}) = 0$, there exists a unique analytic function $\widehat{\tau}^{11}(\widetilde{\Lambda})$ defined on some neighborhood of Λ such that $\widetilde{\tau}^{11} = \widehat{\tau}^{11}(\Lambda)$, so $\widetilde{\tau}^{11}$ is the unique solution for $D = 0$. ■

In the following examples, nonsingularity of $\frac{\partial D}{\partial \tau^{11}}|_{\tau^{11}=0}$ is not verified by the observation that almost no case can make an exception.

4.3.3 Optimization Approach

Before the optimization approach is introduced, the usual quasi-Newton scheme is presented for a comparison, the successive approximation of which is

$$D(\tau^{11(m)}, \Lambda) + D'(\tau^{11(m)}, \Lambda)(\tau^{11(m+1)} - \tau^{11(m)}) = 0, \tag{4.42}$$

where the Jacobian matrix

$$D'(\tau^{11}, \Lambda) = \begin{bmatrix} \frac{\partial D_1(\tau^{11},\Lambda)}{\partial \tau_1^{11}} & \frac{\partial D_1(\tau^{11},\Lambda)}{\partial \tau_2^{11}} & \cdots & \frac{\partial D_1(\tau^{11},\Lambda)}{\partial \tau_N^{11}} \\ \frac{\partial D_2(\tau^{11},\Lambda)}{\partial \tau_1^{11}} & \frac{\partial D_2(\tau^{11},\Lambda)}{\partial \tau_2^{11}} & \cdots & \frac{\partial D_2(\tau^{11},\Lambda)}{\partial \tau_N^{11}} \\ \vdots & \vdots & \vdots & \vdots \\ \frac{\partial D_N(\tau^{11},\Lambda)}{\partial \tau_1^{11}} & \frac{\partial D_N(\tau^{11},\Lambda)}{\partial \tau_2^{11}} & \cdots & \frac{\partial D_N(\tau^{11},\Lambda)}{\partial \tau_N^{11}} \end{bmatrix}. \tag{4.43}$$

If $D'(\tau^{11(m)}, \Lambda)$ is nonsingular, the technique quadratically converges to the solution of $D(\tau^{11}, \Lambda) = 0$ for initial guess close to it. If τ^{11} is close to zero, instead of using $D'(\tau^{11(m)}, \Lambda)$ in (4.42), one can use $D'(0, \Lambda)$ [44]. This quasi-Newton scheme is proven to be efficient.

One difficulty arising for the equation system (4.28) is that $D'(\tau^{11}, \Lambda)$ of it is hard to obtain analytically due to the complicated involvement of τ^{11} in D. Computing

it by a finite difference approach gives

$$[D'(\tau^{11}, \Lambda)]_{mn} = \frac{D_m(\tau^{11} + \varepsilon e_n, \Lambda) - D_m(\tau^{11}, \Lambda)}{\varepsilon}, \tag{4.44}$$

where $[D'(\tau^{11}, \Lambda)]_{mn}$ is the component of $D'(\tau^{11}, \Lambda)$ in the mth row and jth column, D_m is the mth equation of D, e_n is a N-component vector with the component in the nth position being 1 and all other components being 0, and ε is a small quantity usually set to be between 10^{-13} and 10^{-7} [58].

For many other problems, this approximated Jacobian matrix is enough for use. However, for the current one, this is not accurate enough for a convergence of the iteration since the cut-off errors from the components of the matrix easily accumulate and perturb the algorithm seriously. Under the theoretical guarantee of the local existence and uniqueness of a solution from Theorem 4.3.2, another scheme called optimization is utilized to avoid the disadvantage. The structure of this approach is illustrated below.

First, a function[§] for optimization is defined

$$S(\tau^{11}) = \Big(\sum_{i=1}^{K} \sum_{j=1}^{M_{\pi_i}} |D_{\pi_i}(\tau^{11}, \lambda_j)|^{\phi} \Big)^{\varphi} / \sum_{i=1}^{K} M_{\pi_i}, \tag{4.45}$$

where $\varphi > 0$ and $\phi > 0$. In this dissertation, $\varphi = \phi = 1$. If $\widehat{\tau}^{11}$ is the solution of (4.28), it is also a local minimum of $S(\tau^{11})$. The following self-evident theorem illustrates this result more completely.

Theorem 4.3.3 *For K blood pressures, consider $\sum_{i=1}^{K} M_{\pi_i}$ eigenvalues out of them as the form of (4.26) such that $\sum_{i=1}^{K} M_{\pi_i} = N$. The function $S(\tau^{11})$ for optimization*

[§]The function (4.45) for optimization can be constructed in other forms if they make the optimization meaningful and the algorithm run smoothly.

is in the form of (4.45). By these eigenvalues, form a system of N equations as the form of (4.28), which can be verified by Theorem 4.3.2 to have a unique solution in some neighborhood U_0 of $\tau^{11} = 0$. Then $S(\tau^{11})$ has a strict local minimum in the same neighborhood U_0 with the optimal value being 0, i.e. there exists some unique $\tau^{11*} \in U_0$, such that $S(\tau^{11*}) = 0$, and for any $\tau^{11} \in U_0$, $\tau^{11} \neq \tau^{11*}$, $S(\tau^{11}) > S(\tau^{11*})$.

A significant advantage of this approach is that one can over-determine this problem (the quasi-Newton scheme is incapable of realizing this). Namely, in (4.27), consider

$$\sum_{i=1}^{K} M_{\pi_i} > N, \tag{4.46}$$

which means the number of equations in (4.28) is bigger than the number of independent variables. The extra information helps us find the solution more accurately and the algorithm becomes more robust as seen in the following numerous numerical examples. It should be noticed that the minimization for (4.45) from different overestimation produces slightly different τ^{11} where the local minimum occurs. However, the errors from overestimation are small and thus can be ignored.

There are several methods for finding local minima of a function, one of which is Nelder-Mead simplex method [50,51]. It minimizes a function by using only function value without computing any derivative. See Appendix A.4 for an introduction of this method.

The syntax in *Matlab* called *fminsearch* using the Nelder-Mead simplex method as a line search for minimization can be directly employed in our algorithm. The minimal use of it is

$$\text{[Tau, Fun-value]=fminsearch(@S, initial-guess-of-}\tau^{11}\text{)}, \tag{4.47}$$

where '@S' is the function handel for function of (4.45), 'initial-guess-of-τ^{11}' is the initial guess of τ^{11} we input for running of the algorithm, 'Tau' is the output for the vector-valued τ^{11} and 'Fun-value' is the final function value of (4.45) at the output 'Tau'. For detail of this syntax, please reference on Matlab instruction manual.

The fundamental algorithm for using this method is:

Algorithm 4.3.1 *1. For a series of blood pressures, one gains some eigenfrequencies for each of them from IVUS interrogation. Then formulate a function in the form of (4.45);*

2. In MATLAB, by syntax (4.47), run the algorithm and record the output 'Tau' as the vector-valued approximation for τ^{11};

3. By the cubic spline interpolation for 'Tau', compute the final piecewise function approximating τ^{11}.

Two cases are considered. First, we consider the case for τ^{11} in the static deformation equation (3.18) and (3.20) fixed to be the true solution. Hence, the exact r_0 is applied in each inner iteration of the running of the algorithms. This simplification makes the algorithms run fast and is beneficial for devising more viable algorithms. Second, we consider the case for τ^{11} in the static deformation equation not fixed to be the true solution. τ^{11} in the static deformation equation is the same as τ^{11} appearing in other parts for producing the function value of (4.45).

4.3.4 Algorithms for Unknowns Fixed in the Static Deformation

In this section, we will see one significant property of the function (4.45). Then we devise a set of algorithms to search a more accurate solution by various approaches for avoidance of the disadvantages.

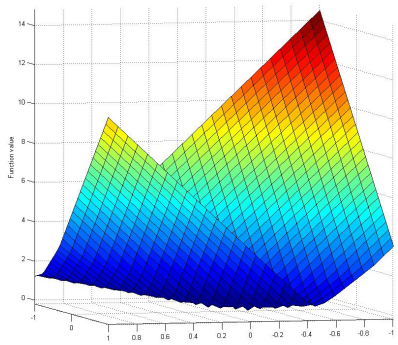

(a) Plot for $\sum_{i=1}^{K} M_{\pi_i} = 8$.

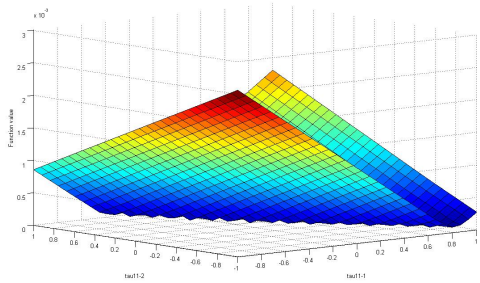

(b) Plot for $\sum_{i=1}^{K} M_{\pi_i} = 12$.

Figure 4.6: Plot of $S(\tau^{11})$ with different values of $\sum_{i=1}^{K} M_{\pi_i}$ for observation of multiple local minima.

4.3.4.1 Multiple Local Minima

The function (4.45) dependent on τ^{11}, consists of the local minimum occurring at the real solution. In addition, multiple local minima densely exist. The following example shows this result.

Example 4.3.4 Consider $\tau^{11} = (\tau_1^{11}, \tau_2^{11})$, which means two independent variables τ_1^{11} and τ_2^{11} are for the function (4.45). The domain is $[-1, 1] \times [-1, 1]$. For Figure 4.6, four blood pressures 90mmHg, 100mmHg, 110mmHg, 120mmHg are used. Two cases are examined. For the first one, there are two eigenvalues for each blood pressure and thus $\sum_{i=1}^{K} M_{\pi_i} = 8$. The plot of function (4.45) is demonstrated in Figure 4.6a. For the second one, there are three eigenvalues for each blood pressure with $\sum_{i=1}^{K} M_{\pi_i} = 12$ and the plot illustrated in Figure 4.6b. For Figure 4.7, nine blood pressures 70mmHg, 80mmHg, 90mmHg, 100mmHg, 110mmHg, 120mmHg, 130mmHg, 140mmHg and 150mmHg are used. Each blood pressure generates only one eigenvalue (the first order eigenvalue). Compared with Figure 4.6, local minima in Figure 4.7 are more sparse and easy to recognize.

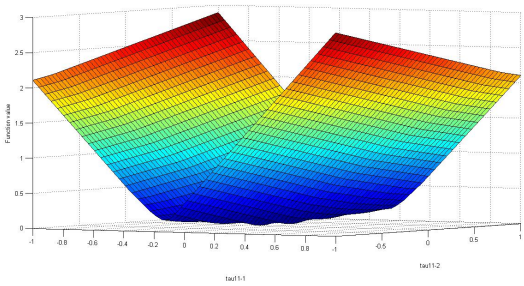

Figure 4.7: Plot of $S(\tau^{11})$ with nine blood pressures (each pressure generates only one eigenvalue) for observation of multiple local minima. This produces less number of local minima.

In Figure 4.6, the multiple local minima in the form of little downward peaks are positioned in the bottom of the two ditch-like figures. They are close to each other and indistinct from their surroundings. This characteristic creates technical difficulties for finding the position of true local minimum. This is why quasi-Newton methods fail to solve the problem, since any initial estimation, however close to the real solution, may lead to a different minimum by the algorithm among so many noisy minima. In the optimization method, relatively more eigenvalues involved in the function 4.45 can enhance the robustness as shown in the following section.

4.3.4.2 Robustness Comparison

In Example 4.3.4, the little peaks in Figure 4.6b are more flattened, and distances between adjacent peaks are also slightly larger than that in Figure 4.6a, where less eigenvalues are used. Therefore, more eigenvalues utilized in function (4.45) help search a more accurate result. The following example can show this conclusion.

Example 4.3.5 We consider $\tau^{11} = (\tau_1^{11}, \tau_2^{11}, \tau_3^{11})$. Six blood pressures 70mmHg, 80mmHg, 90mmHg, 100mmHg, 110mmHg, 120mmHg are used for Figures 4.8a, 4.8b, 4.8d and 4.8e. Four groups of different combinations of these blood pressures and their eigenvalues are listed below:

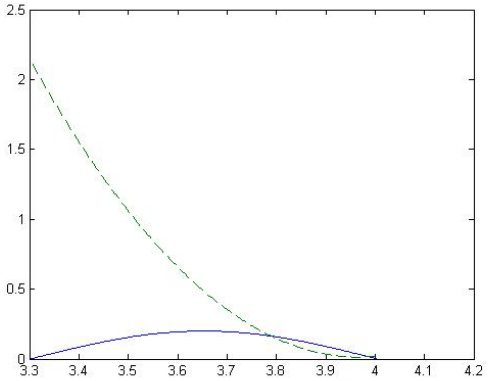

(a) Plot for Group (1).

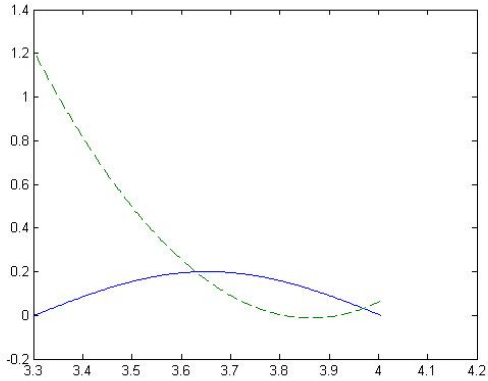

(b) Plot for Group (2).

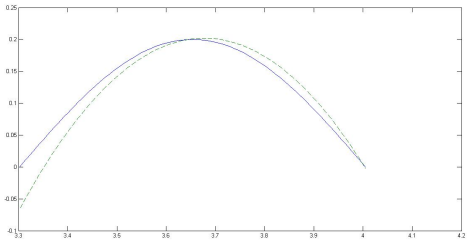

(c) Plot for nine blood pressures with each producing a single eigenvalue.

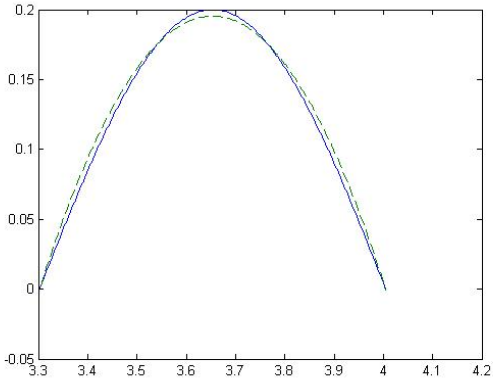

(d) Plot for Group (3).

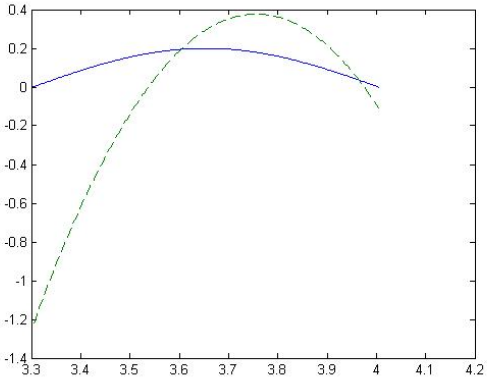

(e) Plot for Group (4).

Figure 4.8: Plots of numerical results for Groups (1)-(4) and the case of nine blood pressures with each one producing a single eigenvalue in Example 4.3.5. The solid line represents the original function and the dashed line represents the approximations.

$$(1): \begin{cases} 90\text{mmHg}: & \lambda_1 \\ 100\text{mmHg}: & \lambda_1 \\ 110\text{mmHg}: & \lambda_1 \\ 120\text{mmHg}: & \lambda_1 \end{cases}; \quad (2): \begin{cases} 70\text{mmHg}: & \lambda_1 \\ 80\text{mmHg}: & \lambda_1 \\ 90\text{mmHg}: & \lambda_1 \\ 100\text{mmHg}: & \lambda_1 \\ 110\text{mmHg}: & \lambda_1, \lambda_2 \\ 120\text{mmHg}: & \lambda_1, \lambda_2 \end{cases};$$

$$(3): \begin{cases} 70\text{mmHg}: & \lambda_1, \lambda_2 \\ 80\text{mmHg}: & \lambda_1, \lambda_2 \\ 90\text{mmHg}: & \lambda_1, \lambda_2 \\ 100\text{mmHg}: & \lambda_1, \lambda_2 \\ 110\text{mmHg}: & \lambda_1, \lambda_2 \\ 120\text{mmHg}: & \lambda_1, \lambda_2 \end{cases}; \quad (4): \begin{cases} 70\text{mmHg}: & \lambda_1, \lambda_2 \\ 80\text{mmHg}: & \lambda_1, \lambda_2 \\ 90\text{mmHg}: & \lambda_1, \lambda_2, \lambda_3 \\ 100\text{mmHg}: & \lambda_1, \lambda_2, \lambda_3 \\ 110\text{mmHg}: & \lambda_1, \lambda_2, \lambda_3 \\ 120\text{mmHg}: & \lambda_1, \lambda_2, \lambda_3 \end{cases};$$

Each group produces an optimization function (4.45) from the blood pressures and its corresponding eigenvalues. The initial estimate for all the five groups is identically $(1, 1, 1)$. The exact function is $\tau^{11}(R) = 0.2\sin(2\pi(R - R_I)/(2L))$. We also consider a special case as shown in Figure 4.8c, where each blood pressure produces only one eigenvalue (the first order eigenvalue), and nine blood pressures 70mmHg, 80mmHg, 90mmHg, 100mmHg, 110mmHg, 120mmHg, 130mmHg, 140mmHg and 150mmHg are used.

In Figure 4.8, we see that Group (3) generates the best approximation. This shows that more terms in (4.45) may make the approximation more accurate, but this is not a guarantee. Group (4) is a counter-example. This may be due to the fact that too much terms in (4.45) can also complicate the computation. Thus, a moderately high number of terms in (4.45) should be considered for higher robustness.

Compare Figure 4.8c with Figure 4.8b, we see that Figure 4.8c produces a better

approximation, where only the first order eigenvalues of all nine blood pressures are used. This means approximation with only first order eigenvalues of each blood pressure could generate better result than higher order eigenvalues used in the algorithm.

4.3.4.3 Error Tolerance in Eigenvalues

In actual measurement for eigenvalues from IVUS implementation, errors are unavoidable. This section demonstrates several examples to see how much errors can be allowed to produce an acceptable approximation. The eigenvalues used in this section are preconditioned (see Section 4.2.3 for topic about "Preconditioning for SLP"). Thus, though the values of frequencies from IVUS implementation are around the order of 10^6 Hz, the actual eigenvalues used in the algorithms are around the order of 10^{-1} Hz for better manipulation by the algorithms.

Example 4.3.6 Nine blood pressures 70mmHg, 80mmHg, 90mmHg, 100mmHg, 110mmHg, 120mmHg, 130mmHg, 140mmHg and 150mmHg are used to produce only the first order eigenvalues for the true function $\tau^{11}(R) = 0.2\sin(2\pi(R - R_I)/(2L))$. The eigenvalues are as follows:

$$\begin{cases} 70\text{mmHg}: & \lambda_1 = 9.308794207954652e-002 \\ 80\text{mmHg}: & \lambda_1 = 1.229315184535560e-001 \\ 90\text{mmHg}: & \lambda_1 = 1.536510111910276e-001 \\ 100\text{mmHg}: & \lambda_1 = 1.852044306524538e-001 \\ 110\text{mmHg}: & \lambda_1 = 2.175236852775457e-001 \\ 120\text{mmHg}: & \lambda_1 = 2.505393118007335e-001 \\ 130\text{mmHg}: & \lambda_1 = 2.841868863592572e-001 \\ 140\text{mmHg}: & \lambda_1 = 3.184084999281991e-001 \\ 150\text{mmHg}: & \lambda_1 = 3.531527004733066e-001 \end{cases};$$

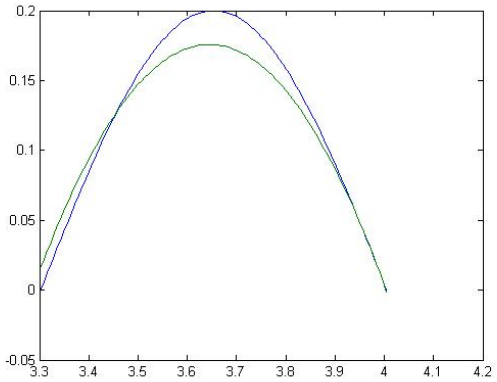

(a) Plot for $K = -12$.

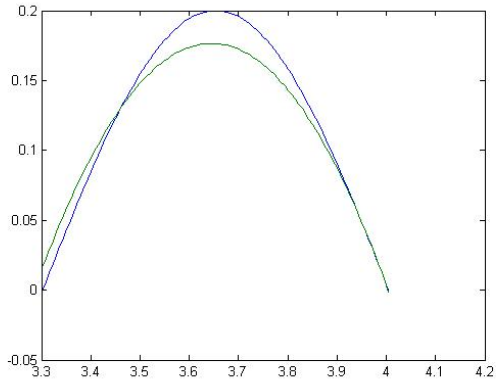

(b) Plot for $K = -10$.

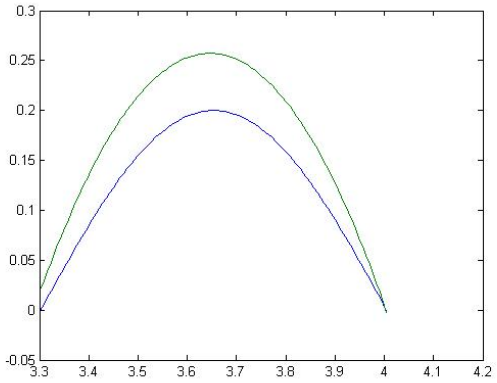

(c) Plot for $K = -8$.

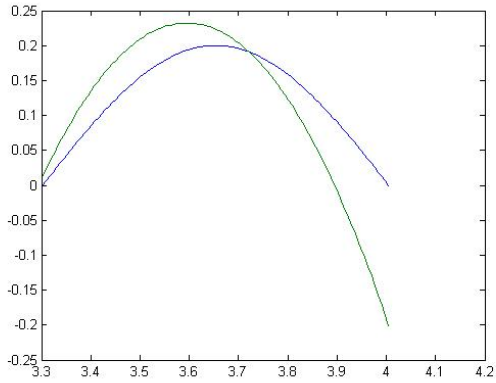

(d) Plot for $K = -7$.

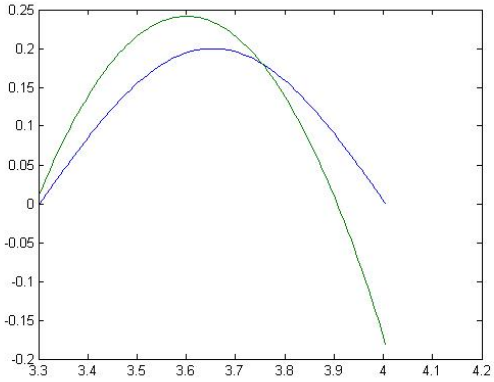

(e) Plot for $K = -5$.

Figure 4.9: Plots of numerical results for various K in Example 4.3.6.

We consider $\tau^{11} = (\tau_1^{11}, \tau_2^{11}, \tau_3^{11})$ to approximate the true solution. Initial input for the optimization is [0.0123 0.223 -0.2]. We add random errors to these eigenvalues (generated by syntax rand(1,1) from MATLAB). Let $\varepsilon \in [0, 1]$ represent the random errors obtained from computer. The actual errors added to these original eigenvalues are $10^K\varepsilon$, where K is negative adjustable integers. The approximations for different K are listed in Figure 4.9. From the plots we can see that as $K < -7$ the approximations are acceptable.

Example 4.3.7 To increase the error tolerance for the algorithms, we employ more eigenvalues and regularization. The true function, number of nodal values used, error interference in the eigenvalues and initial input in the optimization all are the same as in Example 4.3.6. The blood pressures and eigenvalues are as follows:

$$\begin{cases}
70\text{mmHg}: & \lambda_1 = 9.308794207954652e-002 & \lambda_2 = 5.312533556263537e-001 \\
80\text{mmHg}: & \lambda_1 = 1.229315184535560e-001 & \lambda_2 = 7.033010994891145e-001 \\
90\text{mmHg}: & \lambda_1 = 1.536510111910276e-001 & \lambda_2 = 8.799714596154322e-001 \\
100\text{mmHg}: & \lambda_1 = 1.852044306524538e-001 & \lambda_2 = 1.129656275890929e+000 \\
110\text{mmHg}: & \lambda_1 = 2.175236852775457e-001 & \lambda_2 = 1.233454471814210e+000 \\
120\text{mmHg}: & \lambda_1 = 2.505393118007335e-001 & \lambda_2 = 1.437613830833612e+000 \\
130\text{mmHg}: & \lambda_1 = 2.841868863592572e-001 & \\
140\text{mmHg}: & \lambda_1 = 3.184084999281991e-001 & \\
150\text{mmHg}: & \lambda_1 = 3.531527004733066e-001 & \\
160\text{mmHg}: & \lambda_1 = 3.883740179742103e-001 & \\
170\text{mmHg}: & \lambda_1 = 4.240323081114115e-001 & \\
180\text{mmHg}: & \lambda_1 = 4.600921255066295e-001 & \\
190\text{mmHg}: & \lambda_1 = 4.965221687238204e-001 &
\end{cases};$$

To express the approach of regularization (currently from comparison of the output

with true value), we use Π_K to represent the output from the optimization for each K. The output is then divided by an integer factor to obtain a better approximation. As $K = -6$, the new output $\Pi_K/10$ is used in interpolation to generate the approximation. As $K = -5$, the new output $\Pi_K/100$ is used in interpolation to generate the approximation. As $K = -4$, the new output $\Pi_K/1000$ is used. As $K = -3$, the new output $\Pi_K/10000$ is used. See Figure 4.10.

Example 4.3.8 In this example, τ^{11} is fixed to be $\tau^{11}(R) = 0.2\sin(2\pi(R-R_I)/(2L))$. We recover τ^{22} which is a line interval with the true value of $\tau^{22} = \frac{-6(R-R_I)}{R_I-R_O} - 2$. $\tau^{11} = (\tau_1^{11}, \tau_2^{11})$ is utilized to approximate the true solution. Initial input for the optimization is [-2.5 4.5]. The blood pressures and eigenvalues are as follows:

$$\begin{cases} 70\text{mmHg}: & \lambda_1 = 2.555001971506981e-001 & \lambda_2 = 1.640085559374259e+000 \\ 80\text{mmHg}: & \lambda_1 = 2.211609619396642e-001 & \lambda_2 = 1.322237914674498e+000 \\ 90\text{mmHg}: & \lambda_1 = 1.875391777410913e-001 & \lambda_2 = 1.120431298809309e+000 \\ 100\text{mmHg}: & \lambda_1 = 1.547079260764113e-001 & \\ 110\text{mmHg}: & \lambda_1 = 1.227381779339103e-001 & \\ 120\text{mmHg}: & \lambda_1 = 9.166758419102816e-002 & \end{cases};$$

The actual errors added to these original eigenvalues are $10^K\varepsilon$ as in Example 4.3.6, where K is negative adjustable integers. The approximations for different K are listed in Figure 4.11. From the plots we can see that as $K < -5$ the approximations are acceptable.

Example 4.3.8 shows that τ^{22} can tolerate more errors in its eigenvalues than τ^{11} recovery in Example 4.3.6. Thus, the algorithms for τ^{22} are more robust. In practice, τ^{22} is more important than τ^{11} in the bio-mechanical effect for the deformation of the

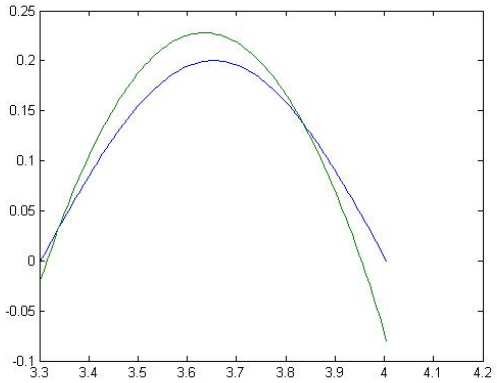

(a) Plot for $K = -6$. The output is divided by a factor of 10 for the interpolation.

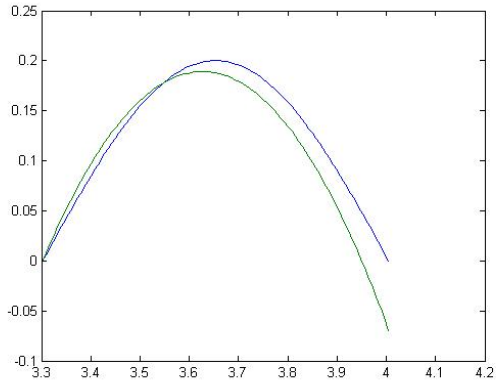

(b) Plot for $K = -5$. The output is divided by a factor of 100 for the interpolation.

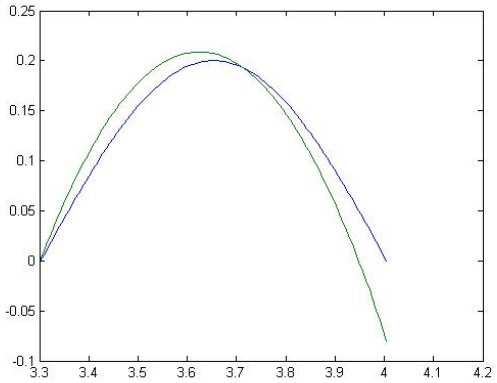

(c) Plot for $K = -4$. The output is divided by a factor of 1,000 for the interpolation.

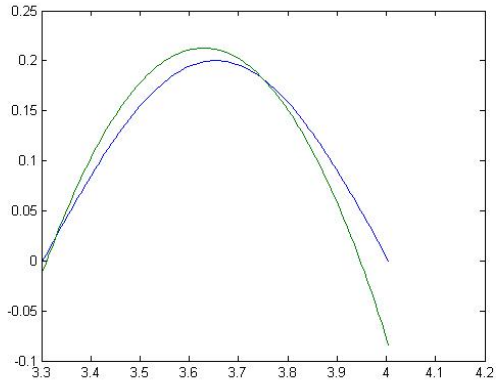

(d) Plot for $K = -3$. The output is divided by a factor of 10,000 for the interpolation.

Figure 4.10: Plots of numerical results for various K in Example 4.3.7. More blood pressures and eigenvalues are used than Example 4.3.6. Regularization is used to produce a better approximation.

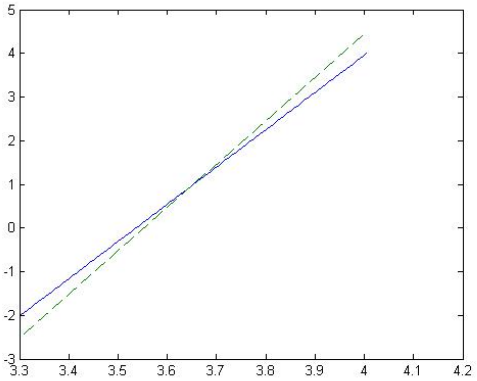

(a) Plot for τ^{22} as $K = -8$.

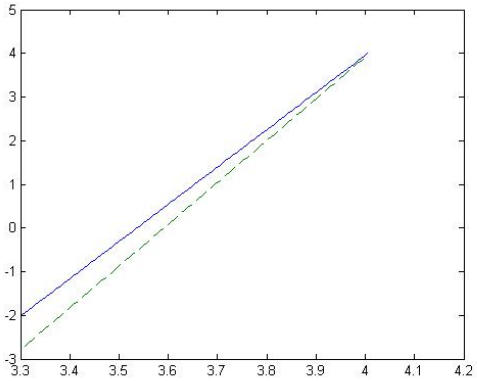

(b) Plot for τ^{22} as $K = -7$.

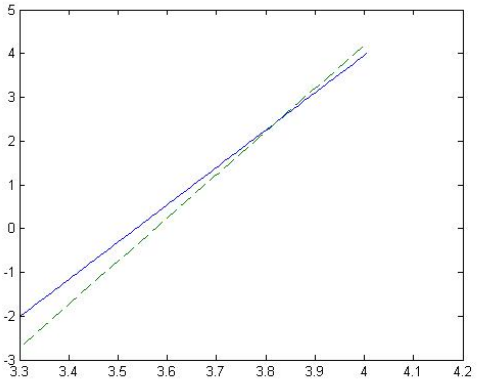

(c) Plot for τ^{22} as $K = -6$.

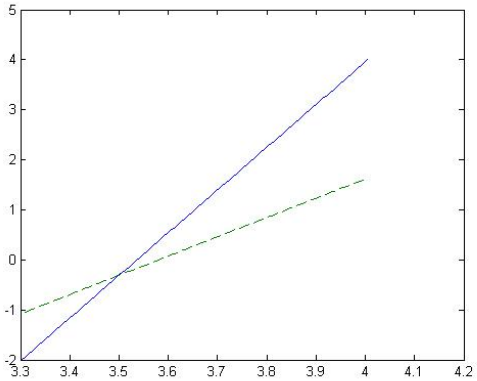

(d) Plot for τ^{22} as $K = -5$.

Figure 4.11: Plots of numerical results for various K in Example 4.3.8.The solid line represents the original function and the dashed line represents the approximations.

blood wall. However, in this thesis, we mainly consider τ^{11} as seen in the following examples to develop more widely applicable algorithms, which can also be utilized for τ^{22} recovery.

4.3.4.4 Enhanced Robustness

The Nelder-Mead simplex method may generate an inaccurate result. More exactly, if we use the previous numerical result as an initial estimation for the algorithm and run it again, it may yield a different output. To obtain a more accurate solu-

tion, We iteratively input the previous numerical result as a new initial guess and run the algorithm until we obtain a limit. Then we use the limit as the final output. The approach can improve the robustness of the algorithm and is displayed as below:

Algorithm 4.3.2 *1. Give an initial guess, run the optimization algorithm and keep a record of the numerical result;*

2. Input the numerical result from Step 1 as a new initial guess and run the algorithm again;

3. Compare the new numerical results from Step 2 and Step 1 to see if they are close to each other;

4. If yes, then stop and accept the numerical result from Step 2 as the final solution; If no, use the numerical result from Step 2 as an initial guess for Step 1 and repeat the process.

Example 4.3.9 In Example 4.3.5, we only use Groups (1) and (4) for optimization. Both of the two initial guesses are set to be $\tau^{11} = (3 \quad 3 \quad 3)$. Relative maximum norm is defined as $\|\tau^{11}_{new} - \tau^{11}_{old}\|_{l^\infty} / \|\tau^{11}_{old}\|_{l^\infty}$, where τ^{11}_{new} is the current numerical result and τ^{11}_{old} is the last one.

From Tables 4.8 and 4.9 and Figure 4.12, we see that after 3 iterations, Group (1) produces a limit far away from the exact one, whereas in the 5 iterations, Group (4) generates output closer and closer to the exact solution. This shows Algorithm 4.3.2 can produce more accurate solution with better robustness if appropriate number of blood pressures and corresponding eigenvalues are selected.

	τ^{11} vector			relative maximum norm
initial guess	3	3	3	
the first output	1.3006	0.3674	0.0107	99.64%
the second output	1.2840	0.3644	0.0120	0.1%
the third output	1.2844	0.3644	0.0120	0%

Table 4.8: Numerical results for Group (1) in Example 4.3.9

	τ^{11} vector			relative maximum norm
initial guess	3	3	3	
the first output	23.5153	-2.7085	3.799	190.28%
the second output	0.8304	0.1658	-0.0447	12.22%
the third output	0.8304	0.1658	-0.0447	102.17%
the fourth output	-0.0184	0.1965	-0.0053	0.05%
the fifth output	-0.0151	0.1963	-0.0054	0.09%

Table 4.9: Numerical results for Group (4) in Example 4.3.9

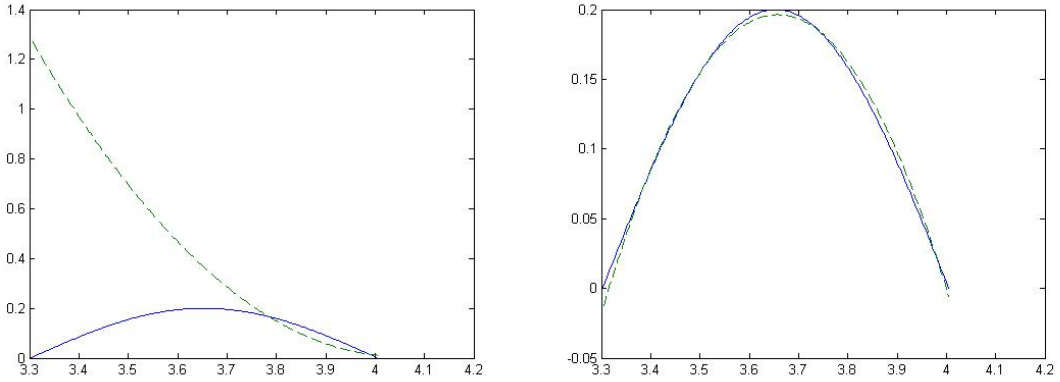

(a) Plot of the final iteration for Group (1). (b) Plot of the final iteration for Group (4).

Figure 4.12: Plots of the final iterations for Groups (1) and (4) in Example 4.3.9. The solid line represents the original function and the dashed line represents the approximations.

4.3.4.5 The Forward Elevated Optimization Algorithm

First, let us see an observation for this optimization problem.

Observation 4.3.1 *If $\widetilde{\tau}^{11}$ is a true solution for the modeling, then for any function (4.45) formed by a combination of blood pressures and the corresponding eigenvalues, $\widetilde{\tau}^{11}$ is always a point producing a local minimum for that function. On the contrary, even though some τ^{*11}, not the true solution for the modeling, exists to be a point generating a local minimum for some functions in the form of (4.45), there always exists a function in the form of (4.45) such that τ^{*11} is not a point for a local minimum for it.*

This observation provides us a technique for estimating the optimization in a forward way. First, for a function (4.45) formed from some group (Γ) of blood pressures and the corresponding eigenvalues, we calculate the optimization and record the output $\tau^{11}_{(1)}$; For another group Δ of blood pressures and the related eigenvalues (Group Δ contains more eigenvalues than Group (Γ)), we input $\tau^{11}_{(1)}$ from Group (Γ) as initial guess and obtain another output $\tau^{11}_{(2)}$; then repeat this process until we find a satisfactory result. Make sure the number of eigenvalues is increased each step to make the method forward. The optimization will produce a result closer and closer to the true solution. The detailed algorithm is as follows:

Algorithm 4.3.3

1. *For an initial guess $\tau^{11}_{(0)}$ and the function (4.45) constructed from a group (Γ) of blood pressures and their eigenvalues, by Algorithm 4.3.1 one obtains the output denoted as $\tau^{11}_{(1)}$;*

2. *Construct a function (4.45) from another group of blood pressures and related eigenvalues denoted as (Δ), where there are more eigenvalues than Group (Γ).*

With $\tau^{11}_{(1)}$ as the input, one finds another output denoted as $\tau^{11}_{(2)}$ by Algorithm 4.3.1;

3. *Construct a function from another group of blood pressures and related eigenvalues denoted as (Θ), where there are more eigenvalues than both (Γ) and (Δ). With $\tau^{11}_{(2)}$ as initial guess, one keep the output $\tau^{11}_{(3)}$ by Algorithm 4.3.1;*

4. *Repeat the forward process until we find a satisfactory result.*

Example 4.3.10 Consider a function $\tau^{11}(R) = (R - \frac{L}{3})(R - R_O)$ to be approximated. We apply the 4-node spline interpolation as $\tau^{11} = (\tau^{11}_1, \tau^{11}_2, \tau^{11}_3, \tau^{11}_4)$. Algorithm 4.3.3 is used as the forward elevated optimization. Group (2) is used to construct the first function. Initial guess is $\tau^{11}_{(0)}$=(0 0 0 0). It produces the output $\tau^{11}_{(1)}$=(0.0202 0.0014 -0.0521 0.0010); Group (3) is used to construct the second function. With $\tau^{11}_{(1)}$ as initial guess, it generates the output $\tau^{11}_{(2)}$=(0.1583 -0.0004 -0.0546 0.0001). This is already a very good result, so we stop and accept this as the final solution. See Figure 4.13 for plots for approximation from $\tau^{11}_{(1)}$ and $\tau^{11}_{(2)}$ respectively. The plot from $\tau^{11}_{(1)}$ does not show a good approximation. The plot for $\tau^{11}_{(2)}$ demonstrates an improvement in approximation.

4.3.4.6 The Backward Comprehensive Test

By the previous several approaches, we can always obtain a final output. Once again to verify it is a satisfactory result, we can apply Observation 4.3.1 to do a backward comprehensive test. The algorithm is as below:

Algorithm 4.3.4 *1. For a function (A) in the form (4.45). By some previous algorithm, we obtain an output $\widetilde{\tau}^{11}$;*

2. *For another function (B), which uses less number of eigenvalues than (A), input $\widetilde{\tau}^{11}$ as an initial guess and obtain another final solution $\tau^{11}_{(1)}$;*

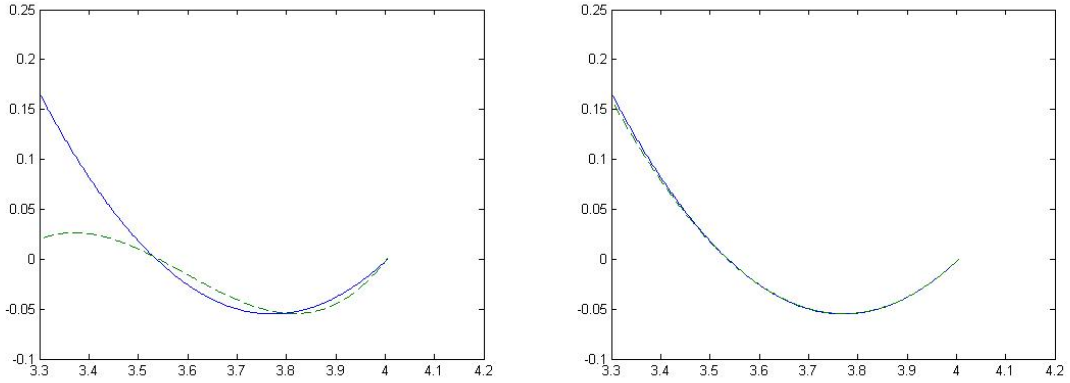

(a) Plot of the first output $\tau^{11}_{(1)}$ of Example 4.3.10.(b) Plot of the second output $\tau^{11}_{(2)}$ of Example 4.3.10.

Figure 4.13: Plots of Example 4.3.10 to show the effect of the elevated optimization algorithm.

3. *For another function (C), which has less number of eigenvalues than (B), we use $\widetilde{\tau}^{11}$ as an initial guess for it and obtain another final solution $\tau^{11}_{(2)}$;*

4. *(Optional) We may use the same way to obtain $\tau^{11}_{(3)}$, $\tau^{11}_{(4)}\cdots$;*

5. *Compare $\tau^{11}_{(1)}$, $\tau^{11}_{(2)}$, $\tau^{11}_{(3)}$, $\tau^{11}_{(4)}\cdots$ with $\widetilde{\tau}^{11}$. If these values are close to each other, then we accept $\widetilde{\tau}^{11}$ as a true solution; if not, $\widetilde{\tau}^{11}$ is not the true solution.*

Example 4.3.11 We consider Example 4.3.9. Group (4) with an initial guess τ^{11}=(3 3 3) generates the final solution $\tau^{11}_{G(4)}$=(-0.0151 0.1963 -0.0054). Then we use this solution as an initial guess for Groups (1), (2) and (3) to obtain the output $\tau^{11}_{G(i)}$ for i=1,2,3 and compute the relative maximum norm defined as: $rmn_i=\|\tau^{11}_{G(4)} - \tau^{11}_{G(i)}\|_{l^\infty}/\|\tau^{11}_{G(4)}\|_{l^\infty}$ for i=1,2,3. The output is as below

$$\underbrace{(-0.0151 \quad 0.1963 \quad -0.0054)}_{\text{output of Group (4) as initial guess}} \Rightarrow \begin{cases} \text{Group (1)}: & (-0.0176 \quad 0.1823 \quad -0.0020) \\ \text{Group (2)}: & (-0.0183 \quad 0.1954 \quad 0.0008) \\ \text{Group (3)}: & (-0.0000 \quad 0.1953 \quad -0.0003) \end{cases}$$

$\underbrace{\text{output of Group (4)}}_{\text{initial guess for Groups (1)-(3)}}$:	(12.9270	-0.3896	-0.6632	0.2311	-0.0011)
output of Group (1):	(-0.5694	-0.0211	0.1502	0.1472	-0.0042)
output of Group (2):	(13.2124	-0.5054	-0.1818	0.0129	-0.0026)
output of Group (3):	(-61.7158	-1.7185	2.5794	1.2377	-0.0077)

Table 4.10: Numerical output for Groups (1), (2) and (3) with initial guess from output of Group (4) in Example 4.3.12. This shows output from Group (4) is a bad approximation.

The relative maximum norms are $rmn_1 = 7.13\%$, $rmn_2 = 1.63\%$, $rmn_3 = 0.51\%$ respectively. The three relative maximum norms are very small and decrease from Group (1) to Group (3). Thus, we can conclude that the output $\tau^{11}_{G(4)}$ from Group (4) is an acceptable approximation of the true solution. Figure 4.14a can show this result.

Example 4.3.12 In 4.3.9, we consider $\tau^{11} = (\tau^{11}_1, \tau^{11}_2, \tau^{11}_3, \tau^{11}_4, \tau^{11}_5)$. Group (4) with an initial guess τ^{11}=(1 2 3 4 5) generates the output $\widetilde{\tau}^{11}_{G(4)}$=(12.9270 -0.3896 -0.6632 0.2311 -0.0011). Then we use this solution as an initial guess for Groups (1), (2) and (3) to obtain the numerical results and compute the relative maximum norm defined in Example 4.3.11. The output is shown in Table 4.10. The relative maximum norms are $rmn_1 = 104.4\%$, $rmn_2 = 1.69\%$, $rmn_3 = 577.42\%$ respectively. They are very big and not close to each other. Consequently, we conclude that $\widetilde{\tau}^{11}_{G(4)}$ is not an acceptable approximation. Figure 4.14b can show this result.

The two examples show the necessity to do a comprehensive test before we accept any final output.

4.3.4.7 The Complete Algorithm and Examples with Other Interpolations

The above algorithms show various approaches to produce a more accurate solution and the corresponding verification. We integrate them and devise a complete

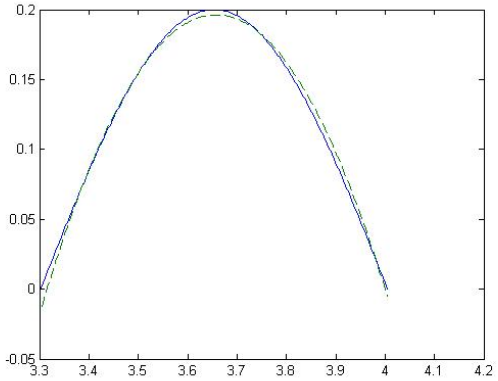

(a) Plot of the result for Group (4) in Example 4.3.11. It shows a good approximation.

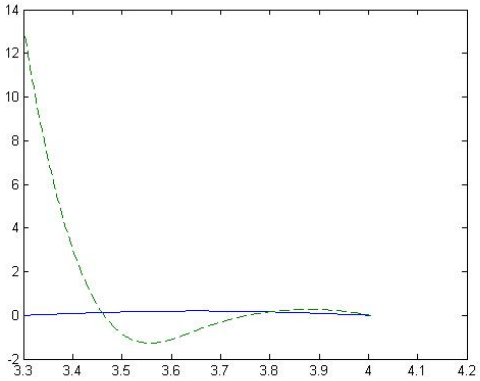

(b) Plot of the output for Group (4) in Example 4.3.12. It shows a bad approximation.

Figure 4.14: Plots of numerical result of Group (4) in Examples 4.3.11 and 4.3.12 to show the necessity of a comprehensive test. The solid line represents the original function and the dashed line represents the approximations.

algorithm.

Algorithm 4.3.5 *1. Construct the function (4.45) under a relation between the number of eigenvalues and number of nodal points as*

$$\sum_{i=1}^{K} M_{\pi_i} = \eta N + \varsigma, \tag{4.48}$$

where M_{π_i} is the number of eigenvalues for the blood pressure π_i, N is the number of nodal points for τ^{11}, the best η can be 4, 5, 6 or bigger to enhance the robustness, and $0 < \varsigma < N$;

2. Use Algorithm 4.3.2 or 4.3.3 to obtain an output, and apply Algorithm 4.3.4 to verify it;

3. If in Step 2 the output from many possible initial guesses does not pass the verification, we need to consider increasing η or ς in (4.48), and go to Step 2;

4. *(Optional) Another way to judge if an approximation is a satisfactory one or not is by observing the function value at the output. Less number of eigenvalues used for the function, less function value should be generated at the output. For example, for N=3 and* $\eta = 6$*, a good approximation may generate a function value as low as* 10^{-7} *.*

Example 4.3.13 The exact function is $\tau^{11} = \sqrt{L^2 - (R - RO)^2}$. The eigenvalues used are based on Group (4). We consider two cases for different number of nodal points:

(a) Set 3 nodes for the interpolation with $\tau^{11} = (\tau_1^{11}, \tau_2^{11}, \tau_3^{11})$. The initial guess is (0 0 0). Algorithm 4.3.2 is utilized. After 4 iterations, the algorithm yields τ^{11}=(0.2417 0.5999 0.7017) with the function value at this point being 3.9595e-008. See Figure 4.15a for the result. From the plot, this output seems not to generate a satisfactory approximation. We consider adding one more node to the interpolation as below in Case (b);

(b) Set 4 nodes for the interpolation with $\tau^{11} = (\tau_1^{11}, \tau_2^{11}, \tau_3^{11}, \tau_4^{11})$. The initial guess is (0 0 0 0) used for the same algorithm as in Case (a). After 5 iterations, the algorithm yields τ^{11}=(0.1407 0.5220 0.6622 0.7069) with the function value at this point being 1.2997e-007. See Figure 4.15b for the approximation. This output produces a much better result than Case (a).

In the dissertation, cubic spline interpolation is mainly used to interpolate the nodal values of τ^{11}. Actually, other interpolations also deserve trying like nearest-neighbor interpolation, linear spline interpolation, piecewise cubic spline interpolation and Hermite interpolation. Different interpolation is suitable for different cate-

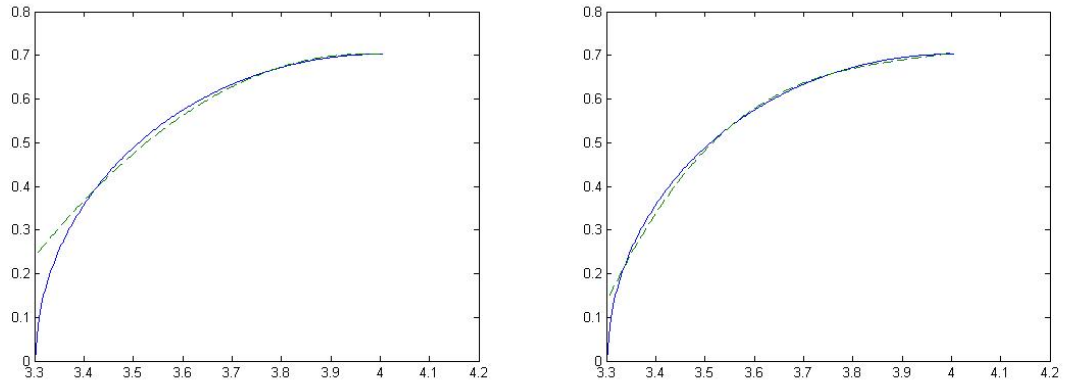

(a) Plot of the output of Example 4.3.13(a). (b) Plot of the output of Example 4.3.13(b).

Figure 4.15: Plots of numerical results of Example 4.3.13 with a monotone function. The solid line represents the original function and the dashed line represents the approximations. Figure 4.15b shows a better approximation with 4 nodes for interpolation than that of Figure 4.15a with a 3-node interpolation, so for different cases, we need to consider different numbers of nodes for interpolation for a better result.

gory of functions. For example, nearest-neighbor interpolation is the best choice for approximating piecewise constant function, and piecewise cubic spline interpolation generates an approximation without the second-time differentiability at the internal nodal points. We mainly make use of cubic spline interpolation for recovering residual stress in the dissertation because component of residual stress as a function in soft tissues is usually smooth. The following two examples show the effect of piecewise cubic spline interpolation.

Example 4.3.14 For the same function in Example 4.3.13 we perform a piecewise cubic interpolation with $\tau^{11} = (\tau_1^{11}, \tau_2^{11}, \tau_3^{11})$. The initial guess is (0 0 0). The output is (0.1844 0.6113 0.7028) and function value at this point is 1.3968e-008. See Figure 4.16.

Example 4.3.15 The exact function is given as $\tau^{11}(R) = 0.1\sin(2\pi(R-RI)/L)$ for a five-node piecewise cubic spline interpolation, where $\tau^{11} = (\tau_1^{11}, \tau_2^{11}, \tau_3^{11}, \tau_4^{11}, \tau_5^{11})$.

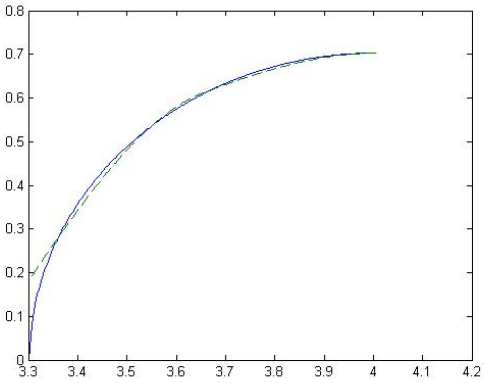

Figure 4.16: Plot of the output of Example 4.3.14. The solid line represents the original function and the dashed line represents the approximations. It shows a better approximation, especially at the left end, than Fig. 4.15a with cubic spline interpolation, so other interpolations other than cubic spline should also be considered.

Eigenvalues used are listed below as Group (5):

$$(5): \begin{cases} 70\text{mmHg}: & \lambda_1, \lambda_2, \lambda_3, \lambda_4 \\ 80\text{mmHg}: & \lambda_1, \lambda_2, \lambda_3, \lambda_4 \\ 90\text{mmHg}: & \lambda_1, \lambda_2, \lambda_3, \lambda_4 \\ 100\text{mmHg}: & \lambda_1, \lambda_2, \lambda_3, \lambda_4 \\ 110\text{mmHg}: & \lambda_1, \lambda_2, \lambda_3, \lambda_4 \\ 120\text{mmHg}: & \lambda_1, \lambda_2, \lambda_3, \lambda_4 \\ 130\text{mmHg}: & \lambda_1, \lambda_2, \lambda_3, \lambda_4 \\ 140\text{mmHg}: & \lambda_1, \lambda_2, \lambda_3, \lambda_4 \\ 150\text{mmHg}: & \lambda_1, \lambda_2, \lambda_3, \lambda_4 \end{cases}$$

The initial guess is (-0.02 0.07 -0.05 -0.05 -0.01). After 2 iterations, it produces the final output (-0.0621 0.0988 -0.0070 -0.0860 -0.0105). Function value at the output is 2.6671e-005. See plot in Fig. 4.17.

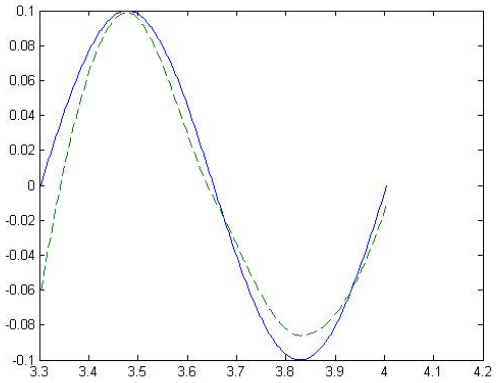

Figure 4.17: Plot of the output of Example 4.3.15. This shows that other interpolation approaches are also possible for use. The solid line represents the original function and the dashed line represents the approximations.

The approximation in Figure 4.17 is not as good as that in the other examples, because five nodes are employed and this increases the complexity when searching for a local minimum. The original function bears two peaks and approximation from less number of nodal points can not properly represent the shape of the function. Hence, 5-node approximation display a relatively better option.

4.3.5 Algorithms for Unknowns not Fixed in the Static Deformation

The algorithms developed in Section 4.3.4 are based on the simplification that the unknown τ^{11} is fixed in the static deformation creating a fixed r_0. The same algorithms can be applied to the situation without such simplification. Namely, r_0 depends on τ^{11} and the iterations in the algorithms also occur in the static deformation. Removal of the simplification makes the problem more ill-posed and highly increases the computational task, but makes the modeling more practical.

The goal is to find the global minimum of the function expressed in (4.45) on some appropriately guessed domain. The global minimum occurs in a very narrow spike of function plot. This makes it uneasy to be searched. To avoid such disadvantage,

we partition the domain into several parts. The Global Optimization Toolbox in MATLAB is utilized to search the global minimum on each subdomain. Draw out a few subdomains where comparatively smaller minima are found. These subdomains are the potential areas where the global minimum in the whole domain occurs. Then we apply the enhanced robustness, the forward elevated optimization algorithm or the backward comprehensive test to find the real τ^{11}. See below for the detailed algorithm

Algorithm 4.3.6 *1. Make an educated guess for the component-wise domain D_i of ${\tau_i}^{11} \in \tau^{11}$ for $1 \leq i \leq N$. This forms a domain $D = D_1 \times D_2 \cdots \times D_N$ of τ^{11}.*

2. Partition D into w subdomains as $D = D^{(1)} \bigcup D^{(2)} \cdots \bigcup D^{(w)}$ (an updated partition should be different from the last one).

3. Use Simulated Annealing method (or other methods like genetic algorithm, pattern search etc. See Global Optimization Toolbox 3 User¡¯s Guide for detail) from the Global Optimization Toolbox of Matlab to search the global minimum on each subdomain.

4. Identify the subdomain $D^{(y)}$ where the global minimum occurring at ${\tau_\mu}^{11} \in D^{(y)}$ is the smallest ($D^{(y)}$ is the potential area where the approximated solution of τ^{11} exists).

5. Form another function in the form (4.45) by more eigenvalues for each blood pressure (or use different blood pressures and corresponding eigenvalues), and utilize Simulated Annealing method (or other global optimization algorithms) to search another global minimum for the new function on $D^{(y)}$ with ${\tau_\mu}^{11}$ as initial guess. Denote the output as ${\tau_\nu}^{11}$.

6. *Compare* ${\tau_\nu}^{11}$ *with* ${\tau_\mu}^{11}$*. If the two are close to each other, go to Step 7 to verify* ${\tau_\nu}^{11}$ *is the true solution; If not, go to Step 2 and repartition the domain* D*.*

7. ${\tau_\nu}^{11}$ *must be verified by Algorithm 4.3.3 or 4.3.4. If the verification succeeds, stop and accept* ${\tau_\nu}^{11}$ *as the true solution. If not, go to Step 2.*

In Step 2, finer partition can generate a better output, but the time for running of the algorithm will be highly increased. Thus, there is always a compromise between accuracy and time. Steps 5, 6 and 7 can be classified as the verification steps to test an output to be the true solution or not. The above algorithm only present one approach. Other verification approaches can also be invented from the basic algorithms of Section 4.3.4. It should be emphasized that the verification is greatly necessary because some global optimization algorithms in Matlab is stochastic and the inverse spectral problem in the modeling is largely ill-posed. Any point other than the true solution, which makes a global minimum occur over a subdomain, can be verified not to be the true solution. The following examples show the flexible employment of Algorithm 4.3.6.

Example 4.3.16 The exact function is given as $\tau^{11}(R) = 5\sin(\pi(R - R_I)/L)$ for a three-node piecewise cubic spline interpolation, where $\tau^{11} = (\tau_1^{11}, \tau_2^{11}, \tau_3^{11})$. The groups of blood pressures and their eigenvalues are listed below.

$$(6): \begin{cases} 70\text{mmHg}: & \lambda_1 \\ 80\text{mmHg}: & \lambda_1 \\ 90\text{mmHg}: & \lambda_1 \\ 100\text{mmHg}: & \lambda_1 \\ 110\text{mmHg}: & \lambda_1 \\ 120\text{mmHg}: & \lambda_1 \\ 130\text{mmHg}: & \lambda_1 \\ 140\text{mmHg}: & \lambda_1 \\ 150\text{mmHg}: & \lambda_1 \end{cases}; \qquad (7): \begin{cases} 70\text{mmHg}: & \lambda_1, \lambda_2, \lambda_3 \\ 80\text{mmHg}: & \lambda_1, \lambda_2, \lambda_3 \\ 90\text{mmHg}: & \lambda_1, \lambda_2, \lambda_3 \\ 100\text{mmHg}: & \lambda_1, \lambda_2, \lambda_3 \\ 110\text{mmHg}: & \lambda_1, \lambda_2, \lambda_3 \\ 120\text{mmHg}: & \lambda_1, \lambda_2, \lambda_3 \\ 130\text{mmHg}: & \lambda_1, \lambda_2, \lambda_3 \\ 140\text{mmHg}: & \lambda_1, \lambda_2, \lambda_3 \\ 150\text{mmHg}: & \lambda_1, \lambda_2, \lambda_3 \end{cases}$$

We suppose $\tau_1^{11} \in [-0.3, \quad 1]$, $\tau_2^{11} \in [-0.3, \quad 5.3]$ and $\tau_3^{11} \in [-0.3, \quad 1]$. We partition the whole domain $[-0.3, \quad 1] \times [-0.3, \quad 5.3] \times [-0.3, \quad 1]$ into five subdomains as

$$\begin{cases} \textcircled{1}: & [-0.3, \quad 1] \times [-0.3, \quad 1] \times [-0.3, \quad 1] \\ \textcircled{2}: & [-0.3, \quad 1] \times [1, \quad 2] \times [-0.3, \quad 1] \\ \textcircled{3}: & [-0.3, \quad 1] \times [2, \quad 3] \times [-0.3, \quad 1] \\ \textcircled{4}: & [-0.3, \quad 1] \times [3, \quad 4] \times [-0.3, \quad 1] \\ \textcircled{5}: & [-0.3, \quad 1] \times [4, \quad 5.3] \times [-0.3, \quad 1] \end{cases}$$

On the five subdomains, we search the global minima respectively with Group (6) by algorithm of Simulated Annealing. The time running on each subdomain is equally set to be 10 minutes. The outputs are in Table 4.11. We can see that subdomain $\textcircled{5}$ generates the smallest function value with an order of 10^{-5}. This implies that the global minimum of the whole domain occurs most possibly on this subdomain.

To further study this subdomain completely, we design another function for optimization by Group (7), where the number of eigenvalues are tripled compared with Group (6). On subdomain $\textcircled{5}$, we use [0.1 4.9 0.1] as input, the algorithm by Sim-

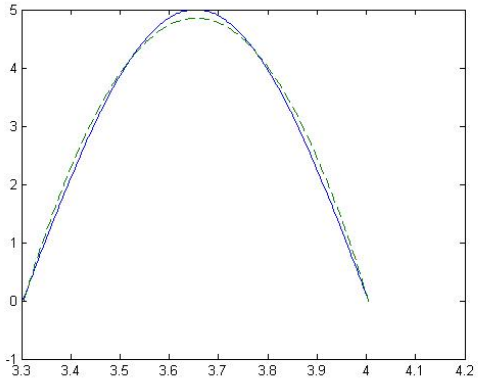

Figure 4.18: Plot of the approximation of Example 4.3.16. The solid line represents the original function and the dashed line represents the approximations.

ulated Annealing with Nelder-Meader simplex as a hybrid gives a global minimum 5.4928e-5 occurring at [-0.0777 4.9 -0.025].

[-0.0777 4.9 -0.025] should be verified to be the approximated true solution. By the approach of enhanced robustness from Section 4.3.4.4, we use [-0.0777 4.9 -0.025] as input under algorithm of Simulated Annealing with hybrid of Nelder-Mead simplex method over the domain $[-0.2, \quad 0.2] \times [4.8, \quad 5.2] \times [-0.2, \quad 0.2]$ closely around [-0.0777 4.9 -0.025]. The minimum 1.144e-007 of the function occurs at [-0.067155 4.8528 -0.013693]. [-0.0777 4.9 -0.025] and [-0.067155 4.8528 -0.013693] are close to each other. Hence we can certify that [-0.067155 4.8528 -0.013693] is the desired approximation. See Figure 4.18 for the plots of the real function and the approximation. The forward elevated optimization algorithm and the backward comprehensive test can still be used to test the accuracy of the solution.They are ignored for succinctness.

Example 4.3.17 The exact function is $\tau^{11}(R) = 100(R - R_I)^2(R - R_O) + 5.5$ for a three-node piecewise cubic spline interpolation, where $\tau^{11} = (\tau_1^{11}, \tau_2^{11}, \tau_3^{11})$. We suppose $\tau_1^{11} \in [5, \quad 6]$, $\tau_2^{11} \in [1, \quad 1.5]$ and $\tau_3^{11} \in [5, \quad 6]$. We partition the whole

subdomain	initial input	global minimum
①	[0.35 0.35 0.35]	1.6308e-3 occurring at [0.6913 0.0262 0.0359]
②	[0.35 1.5 0.35]	1.3326e-3 occurring at [0.7730 1.7268 0.0557]
③	[0.35 2.5 0.35]	1.4648e-3 occurring at [1 2.8167 -0.0020]
④	[0.35 3.5 0.35]	5.9577e-4 occurring at [0.3985 3.5800 0.0162]
⑤	[0.1 4.9 0.1]	9.0288e-5 occurring at [0.90649 4.3238 -0.0006]

Table 4.11: Numerical results for Example 4.3.16

domain $[5, \quad 6] \times [1, \quad 1.5] \times [5, \quad 6]$ into three subdomains as

$$\begin{cases} ①' : & [5, \quad 5.2] \times [1, \quad 1.5] \times [5, \quad 6] \\ ②' : & [5.2, \quad 5.8] \times [1, \quad 1.5] \times [5, \quad 6] \\ ③' : & [5.8, \quad 6] \times [1, \quad 1.5] \times [5, \quad 6] \end{cases}$$

On the three subdomains, we search the global minima respectively for function formed from Group (6) by algorithm of Simulated Annealing with hybrid of Nelder-Mead simplex method. The results are in Table 4.12. We can see that subdomain ②′ generates the smallest function value with an order of 10^{-11}. This implies that the global minimum of the whole domain occurs most possibly on this subdomain.

We use Nelder-Mead simplex algorithm with [5.6330 1.1688 5.5000] as input. It gives the minimal function value 2.8548e-011 at the point [5.6330 1.1688 5.5000]. The input and output are almost the same. This shows that [5.6330 1.1688 5.5000] should be the final solution of the approximation. To further test this result, we design another function for optimization by Group (7), and Nelder-Mead simplex algorithm with [5.6330 1.1688 5.5000] as input is applied again. The function minimum 5.2509e-005 occurs at [5.6340 1.1805 5.5000]. The output is only slightly different from the input. This shows that [5.6330 1.1688 5.5000] is the approximated solution as claimed. See Figure 4.19 for the comparison of true solution and its approximation.

subdomain	initial input	global minimum
①′	[5.1 1.3 5.8]	8.0149e-010 occurring at [5.1893 1.0016 5.5001]
②′	[5.3 1.2 5.5]	2.8554e-011 occurring at [5.6330 1.1688 5.5000]
③′	[5.9 1.4 5.3]	3.1077e-010 occurring at [5.9641 1.0791 5.5001]

Table 4.12: Numerical results for Example 4.3.17

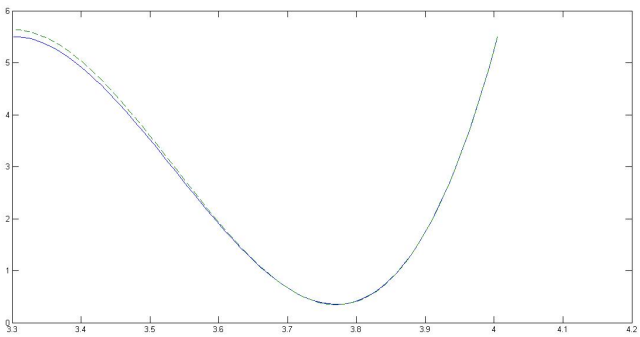

Figure 4.19: Plot of the approximation of Example 4.3.17. The solid line represents the original function and the dashed line represents the approximations.

5. SUMMARY

At the end, a summary is presented. Discussions are made for the modeling and algorithms developed in the dissertation. The contributions of the research in the dissertation are also summarized. Short-term and long-term plans are displayed for the future research to complete the project.

5.1 Discussions

This section shows why the algorithms are devised and what the benefits they are compared to other approaches.

5.1.1 Discussions for Recovering the Shear Modulus

The shear modulus is one of several quantities for measuring the stiffness of arterial wall. Its recovery is crucial for studying the bio-mechanical properties of the wall. The extent of hardening of an atherosclerotic plaque is known to depend on shear modulus. Therefore, methods to accurately estimate values of shear modulus can contribute in distinguishing between a healthy artery and an unhealthy one. Traditionally, one needs experiments in vitro to recover shear modulus [7]. However, the method presented in this article provides a novel way to measure it from IVUS implementation in vivo. It is also known that the shear modulus in soft tissues is not constant, and it varies within the thickness of the arterial wall. The cubic spline interpolation can give us flexibility for finding different values on different layers of the wall, which makes the result more practical.

A novelty in our work is that we use a nonlinear system of equations from various blood pressures instead of one linear equation from only one pressure. This engenders a nonlinear approach for the problem. It complicates the theoretical work but makes

the result more accurate by featuring the nonlinear characteristic of the problem.

Large N, which is the number of nodal points of the recovered functions, generally makes it difficult for the algorithm to be both robust and accurate. We also tried other methods to replace the generalized secant method such as Broyden's method in [2], but the results are not so satisfactory. Other algorithms deserving trial may complicate the problem, e.g. Newton-Krylov method [3, 58] and inexact Newton method [19]. Solving nonlinear simultaneous equations efficiently and accurately is still a challenging problem today. Most of these methods are variation of Newton's method which requires computing the Jacobian matrix. However, it is almost impossible to obtain the Jacobian matrix for many highly nonlinear problems. Our problem is even more complicated due to the fact that there are no explicit formulas for $d_j(\mu)$ in (4.12). Most of the existing methods for solving this kind of problem depends on finding an approximate Jacobian matrix. The method that we present is very easy to implement and avoids having to approximate the Jacobian matrix.

The idea of the algorithm can be applied to recover other constants like β, π, R_I or R_O given all the relevant information. For the atherosclerotic plaques with two layers, one of which is soft and fatty and the other one calcified and fibrous, we can also utilize this algorithm to find the position of the interface of the two layers.

5.1.2 Discussions for Recovering the Residual Stress

Biologically, it is not likely that any soft tissue can be completely free from residual stress introduced during growth. Residual stress can be beneficial in maintaining the healthy state of an artery. It can also be detrimental when it reduces the stability of the material which may cause, for example, a vulnerable atherosclerotic plaque to rupture suddenly. This article incorporates residual stress analytically in the arterial modeling and recovers the stress distribution of some components of it via an inverse

spectral technique. Due to the characteristic of multiple local solutions of the problem, the approach of solving a system of equations is avoided. Instead, a function is constructed for optimization to obtain the solution. A forward elevated optimization and backward comprehensive test are employed to increase the robustness and guarantee the accuracy of the output.

In addition, the inverse spectral technique does not operate on the original SLP form. Instead, it works on one of the first order differential equations after the application of prüfer transformation. The advantage of this performance is that one boundary condition of the new form relates to the eigen-order, thus providing extra vital information for the calculation.

Usually, solving a system of equations is employed to find the solution of equations established by the inverse spectral technique. However, some facts make such approach impossible as analyzed in Section 5.1.1. First, the Jacobian matrix is hard to obtain analytically and the approximated one is inaccurate for use, resulting a divergence of the algorithm. Second, some points near the true solution also make the system of equations close to zero, so any Newton-like approach will easily converge to the points which are not the solution. Instead, optimization technique is utilized. Many algorithms for optimization, like the Nelder-Mead simplex method, can search the solution directly without any use of the gradient of the function. The over-estimation of the problem in the optimization also increases the capability of distinguishing the solution from other noisy data.

5.2 Summary of Contributions

The proposed research makes several contributions to biomedical engineering. First of all, IVUS is proposed as a method for obtaining the natural frequencies of the arterial wall. Second, the shear modulus as a function is recovered to represent

the variation of stiffness along the radial direction. Third, the inverse spectral approach in the research establishes an analytical way to estimate the residual stress more accurately. Current practice for experimentally measuring residual stress is done by cutting a slice of arterial ring radially, where the ring segment springs open to minimize its stored energy by relieving the residual stress. This in vitro technique is inaccurate since additional cutting causes a redistribution of residual stress. Fourth, usually, only one blood pressure is utilized to obtain a sequence of eigenvalues. In this research, several different blood pressures are employed, each of which generates several eigenvalues. This makes the nature of the governing differential equations nonlinear, which is more applicable and accurate because more blood pressures involved produce more information for the computing, and the lower-mode eigenfrequencies are easier to be detected and also more accurately estimated from experiment.

The research also contributes to inverse spectral techniques. First, reverse use of cubic spline interpolation for inverse problem is applied. Traditionally, given values at nodes, one can interpolate them by cubic splines. In the inverse problem, the values at nodes are unknown and one needs to calculate them so that the splines from interpolation can approximate a function appropriately. Second, a multi-dimensional secant algorithm is built up for inverse SLP to recover unknown function, which is usually done by method from fixed-point theorem. Third, instead of using a standard quasi-Newton approach for finding solutions of a system of equations, an optimization approach is utilized for calculating the solution, and the overestimation makes the algorithms more robust.

5.3 Future Research Plan

The long-term goal of the project in the dissertation is to discriminate the stable atherosclerotic plaques from unstable ones. The research in the dissertation serves as a foundation for understanding the structure of the modeling and inverse spectral techniques so that we can establish more complicated models for more practical realizations. Future studies need to test the effectiveness of the modeling and inverse spectral techniques by experimental data.

5.3.1 Short-term Plan

As shown in Section 4.3.4.3, the algorithms developed are sensitive to the errors in the eigenfrequencies for both τ^{11} and τ^{22} recovery. This is natural because most of the inverse problems are ill-posed and sensitive to the initial data. For in vitro experiments in lab operating on phantom materials, the indicated eigenfrequency measurement accuracy can be achieved much more easily than in vivo measurements of soft tissue. As done for many other inverse problems, future work needs to construct an effective regularization or design more effective algorithms for the inverse reconstructions demanding less stringent eigenfrequency measurement accuracy requirements.

The constitutive model we use in Section 3.2 was proposed by Ronald Rivlin in 1948. This model comes from statistical thermodynamics of plastic and rubber-like materials due to the cross-linked polymer chains effect. The stress-strain behavior of hyperelastic material under this model is nonlinear. And arterial wall belongs to this category. The disadvantage of this model is that it works better for low strain of the material. Experiments on arteries suggest that stress-strain behavior should be modeled using exponential stiffening with increasing strain [11], and that such strong nonlinear response should cause the inverse spectral methods to be more accurate.

To better reflect the structure of blood vessels, the arterial wall will be modeled as an anisotropic material, where two families of collagen fibres are embedded in an isotropic groundmatrix. Collagen fibres are key factors of the architecture of the arterial wall. Continuum models for the arterial model showing the effect of collagen fibres accounts for more accurate mechanical distribution. The natural strain energy function used to derive the Piola-Kirchhoff stress is a superposition of the isotropic potential for the non-collagenous groundmatrix and the two transversely isotropic potentials for the embedded families of collagen fibres. There is a total of ten neo-Hooken and fibre-orientation parameters. Inverse methods are established to recover most of the key parameters while the less significant ones are given from educated guesses. Second, for the pathological arterial wall with atherosclerotic plaques, we consider a two layered arterial wall. One represents the softer, fatty core formed initially, and the other one represents the harder, fibrous layer formed later covering the core. The two layers possess different material parameters, and the thickness of the two layers are not uniform in the angular direction. We will use the spectrum gained from the IVUS interrogation to recover the shear modulus and thickness of each layer. The layer thickness suggests whether or not the later formed layer is thick enough to prevent the sudden rupture of the atherosclerotic plaques. Third, we will consider the multiplicative model instead of the additive model for how the residual stress is involved in the Cauchy stress. There is no conclusion for how the two stresses are involved theoretically or practically, so we can utilize different forms to see which one better simulates the experimental data.

5.3.2 Long-term Plan

A three dimensional ultrasound wave is considered to spread inside the artery. Thus, the vibration of the arterial wall is also three dimensional, and three eigen-

modes in the three cylindrical directions need to be utilized. The boundary value problems for both the static deformations and vibration caused deformations produce highly complicated partial differential equations. These equations are utilized to recover material parameters, residual stress, thickness of layers and so on. Then incorporating these recovered quantities, we will construct a complete mathematical approach for the distinguishment of two types of atherosclerotic plaques from the information of natural frequencies gained from the IVUS interrogation.

The biological modeling will bring more challenging numerical problems to the research. We will apply approaches from numerical analysis and scientific computing to analyze some special partial differential equations and find the corresponding numerical solutions. As well, under our theoretical work, we need to validate the modeling and inverse spectral approaches. We propose utilizing phantom material to imitate the in-vivo arterial wall. The IVUS interrogation inside such material is used to generate natural material frequencies. Then the spectral data are used as input to test the effectiveness of the modeling. Finally, we will consider applying the model to in-vivo arteries for the ultimate goal to distinguish atherosclerotic plaques.

REFERENCES

[1] Cowin, S., Doty, S. Tissue mechanics, Springer, New York, 2010.

[2] Broyden, C. G. A class of methods for solving nonlinear simultaneous equations. Mathematics of Computation, 19, 577-583(1965).

[3] Brown, P. N., Saad, Y. Hybrid krylov methods for nonlinear systems of equations. SIAM Journal on Scientific Computing, 11, 450-481(1990).

[4] Casscells, W., Naghavi, M., Willerson, J. T. Vulnerable atherosclerotic plaque: a multifocal disease. Circulation, 107, 2072-2075(2003).

[5] Chuong, C. J., Fung, Y. C. Compressiblity and constitutive equation of arterial wall in radial compression experiments. Journal of Biomechanics, 17, 35-40(1984).

[6] Chuong, C. J., Fung, Y. C. Residual stress in arteries, in: Schmid-Schoëbein, G. W., Woo, S. L.-Y., Zweifach, B. W. (Eds.), Frontiers in Biomechanics. Springer-Verlag, New York, pp. 117-129(1986).

[7] Deng, S. X., Tomioka, J., Debes, J. C., Fung, Y. C. New experiments on shear modulus of elasticity of arteries. American Physiological Society, 266, H1-H10(1994).

[8] Fabiano, R. H., Knobel, R. K., Lowe, R. D. A finite-difference algorithm for an inverse Sturm-Liouville problem. IMA Journal of Numerical Analysis, 15, 75-88(1993).

[9] Fung, Y. C. What principle governs the stress distribution in living organ? in: Fung, Fukada, Wang, (Eds.), Biomechanics in China, Japan and USA. Science Press, Beijing, pp. 1-13(1983).

[10] Fung, Y. C. Biomechanics: mechanical properties of living tissues, Springer, New York, 1993.

[11] Gasser, T. C., Ogden, R. W., Holzapfel, G. A. Hyperelastic modeling of arterial layers with distributed collagen fibre orientations. Journal of the Royal Society Interface 3, 15-35(2006).

[12] Hodgson, J., Reddy, K., Suneja, R., et al. Intracoronary ultrasound imaging: correlation of plaque morphology with angiography, clinical syndrome and procedural results in patients undergoing coronary angioplasty. Journal of the American College of Cardiology, 21, 35-44(1993).

[13] Hoger, A. On the residual stress possible in an elastic body with material symmetry. Archive for Rational Mechanics and Analysis, 88, 271-289(1985).

[14] Hoger, A. On the determination of residual stress in an elastic body. Journal of Elasticity, 16, 303-324(1986).

[15] Holzapfel, G. A. Nonlinear solid mechanics. A continuum approach for engineering, first edition, Wiley, Chichester, 2000.

[16] Holzapfel, G. A., Ogden, R. W. Biomechanics of soft tissues in cardiovascular systems, Springer, New York, 2004.

[17] Humphrey, J. D. Cardiovascular solid mechanics: cells, tissues, and organs, Springer, New York, 2010.

[18] Johnson, B. E., Hoger, A. The dependence of the elasticity tensor on residual stress. Journal of Elasticity, 33, 145-165(1993).

[19] Kelley, C. T. Iterative methods for linear and nonlinear equations, SIAM, Philadelphia, 1995.

[20] Kincaid, D., Cheney, W. Numerical analysis: mathematics of scientific computing, Brooks Cole, Pacific Grove, 2002.

[21] Loree, H. M., Grodzinsky, A. J., Park, S. Y., Gibson, L. J., Lee, R. T. Static circumferential tangential modulus of human atherosclerotic tissue. Journal of Biomechanics, 27, 195-204(1994).

[22] Masson, I., Fassot, C., Zidi, M. Finite dynaic deformations of a hyperelastic, anisotropic, incompressible and prestressed tube. Applications to in vivo arteries. European Journal of Mechanics - A/Solids, 29, 523-529(2010).

[23] Wang, Y., Hsu, T., Jan, M., Wang, W. Review: theory and applications of the harmonic analysis of arterial pressure pulse waves. Journal of Medical and Biological Engineering, 30, 125-131(2010).

[24] Wolfe, P. The Secant method for simultaneous nonlinear equations. Communications of the ACM, 2, 12-13(1959).

[25] Bergel, D.H. The visco-elastic properties of the arterial wall, Ph. D thesis, University of London, London, 1960.

[26] Fung, Y.C. What are the residual stresses doing in our blood vessels? Annals of Biomedical Engineering, 19, 237-249(1991).

[27] Gorb, Y., Walton, J.R. Dependence of the frequency spectrum of small amplitude vibrations superimposed on finite deformations of a nonlinear, cylindrical

elastic body on residual stress. International Journal of Engineering Science, 48, 1289-1312(2010).

[28] Gou, K., Joshi, S., Walton, J.R. Recovery of the shear modulus of hyperelastic soft tissue by an inverse spectral technique. International Journal of Engineering Science, 56, 1-16(2012).

[29] Lanir, Y. Mechanisms of residual stress in soft tissues. Journal of Biomedical engineering, 131, (2009).

[30] Potkin, B., Bartorelli, A., Gessert, J. et al. Coronary artery imaging with intravascular high-frequency ultrasound. Circulation, 81, 1575-1585(1990).

[31] Bhadeshia, H. Residual stress: material factors, in: G. Totten, M. Howes, T. Inoue, (Eds.), Handbook of residual stress and deformation of steel. ASM International, Materials Park, Ohio, pp. (3-10)2002.

[32] Hoger, A. Residual stress in an elastic body: a theory for small strains and arbitrary rotations. Journal of Elasticity, 31, 124(1993).

[33] Johnson, B.E., Hoger, A. The use of a virtual configuration in formulating constitutive equations for residually stressed elastic materials. Journal of Elasticity, 41, 177-215(1995).

[34] Raghavan, M.L., Trivedi, S., Nagarau, A., Mcpherson, D.D., Chandran, K.B. Three-dimensional finite element analysis of residual stress in arteries. Annals of Biomedical Engineering, 32, 257-263(2004).

[35] Humphrey, J.D. Vascular adaptation and mechanical homeostasis at tissue, cellular, and sub-cellular levels. Cell Biochemistry and Biophysics, 50, 53-78(2007)

[36] Rodriguez, E.K., Hoger, A., McCulloch, D.A. Stress dependent finite growth in soft elastic tissues. Journal of Biomechanics, 27, 455-467(1994).

[37] Gou, K., Walton, J.R. Reconstruction of residual stress as functions for soft hyperelastic tissue via an inverse spectral technique by optimization. Mathematics and Mechanics of Solids, submitted.

[38] Skalak, R., Zargaryan, S., Jain, R., Netti, P., Hoger, A. Compatibility and the genesis of residual stress by volumetric growth. Journal of Mathematical Biology, 34, 889-914(1996).

[39] Gou, K., Sun, B. Numerical solution of the Goursat problem on a triangular domain with mixed boundary conditions. Applied Mathematics and Computation, 217, 8765-8777(2011).

[40] Greenwald, S.E., Moore, J.E., Rachev, A., Kane, T.P.C., Meister, J.J. Experimental investigation of the distribution of residual strains in the artery wall. Journal of Biomechanical Engineering, 119, 438-444(1997).

[41] Cardamone, L., Valentn, A., Eberth, J.F., Humphrey, J.D. Origin of axial prestretch and residual stress in arteries. Biomechanics and Modeling in Mechanobiology, 8, 431-446(2009).

[42] Zeller, P.J., Skalak, T.C. Contribution of individual structural components in determining the zero-stress state in small arteries. Journal of Vascular Research, 35, 8-17(1998)

[43] Nissen, S.E., Gurley, J.C., Grines, C.L., Booth, D.C., McClure, R., Berk, M., Fischer, C., DeMaria, A.N. Intravascular ultrasound assessment of lumen size

and wall morphology in normal subjects and patients with coronary artery disease. American Heart Association, Circulation, 84, 1087-1099(1991).

[44] Lowe, B.D., Pilant, M., Rundell, W. The recovery of potentials from finite spectral data. SIAM Journal on Mathematical Analysis, 23, 482-504(1992).

[45] Bailey, P.B., Everitt, W.N., Zettl, A. Algorithm 810: the Sleign2 Sturm-Liouville code. ACM Transactions on Mathematical Software, 27, 143-192(2001).

[46] Holzapfel, G.A., Gasser, T.C., Ogden, R.W. A new constitutive framework for arterial wall mechanics and a comparative study of material models. Journal of Elasticity, 61, 1-48(2000).

[47] Pryce, J.D. Numerical solution of Sturm-Liouville problem, Clarendon Press, Oxford, 1993.

[48] Rickenbacher, P. Role of intravascular ultrasound versus angiography for diagnosis of graft vascular disease. Transplantation Proceedings , 30, 891-892(1998).

[49] Vince, D.G., Dixon, K.J., Cothren, R.M., Cornhill, J.F. Comparison of texture analysis methods for the characterization of coronary plaques in intravascular ultrasound images. Computerized Medical Imaging and Graphics, 24, 221-229(2000).

[50] Lagarias, J.C., Reeds, J.A., Wright, M.H., Wright, P.E. Convergence properties of the Nelder-Mead simplex method in low dimensions. SIAM Journal on Optimization, 9, 112-147(1998).

[51] Nelder, J.A., Mead, R. A simplex method for function minimization. Computer Journal, 7, 308-313(1965).

[52] Holzapfel, G.A., Sommer, G., Auer, M., Regitnig, P., Ogden, R.W. Layer-specific 3D residual deformations of human aortas with non-atherosclerotic intimal thickening. Annals of Biomedical Engineering, 35, 530-545(2007).

[53] Lu, X., Pandit, A., Kassab, G.S. Biaxial incremental homeostatic elastic moduli of coronary artery: two-layer model. American Journal of Physiology - Heart and Circulatory Physiology, 287, 1663-1669(2004).

[54] Carlier, S.G., Tanaka, K., Katouzian, A., Mintz, G.S. Atherosclerotic plaque characterization from radio frequency ultrasound signal processing. Imaging Ultrasound, 54-56(2007).

[55] Jeremias, A., Kolz, M., Ikonen, T.S., Gummert, J.F., Oshima, A., Hayase, M., Honda, Y., Komiyama, N., Berry, R.E., Morris, G.J., Yock, P.G., Fitzgerald, P.J. Feasibility of in vivo intravascular ultrasound tissue characterization in the detection of early vascular transplant rejection. Circulation, 100, 2127-2130(1999).

[56] Rundell, W., Sacks, P.E. Reconstruction techniques for classical inverse Sturm-Liouville problems. Mathematics of Computation, 58, 161-183(1992).

[57] Rundell, W., Sacks, P.E. The recosntruction of Sturm-Liouville operators. Inverse problems, 8, 457-482(1992).

[58] Kelley, C. T. Solving nonlinear equations with Newton's method, SIAM, Philadelphia, 2003.

APPENDIX A

SOME BASIC ALGORITHMS

A.1 Runge Kutta Formula for Initial Value Problem

Now suppose we encounter a second order differential equation with initial values

$$x''(t) = f(t, x, x'), \quad \text{for} \quad t \geq a, \tag{A.1}$$

$$x(a) = \alpha, \tag{A.2}$$

$$x'(a) = \beta, \tag{A.3}$$

where f is a known function and α and β are known constants [20]. We set

$$x_1 = t, \quad x_2 = x(t), \quad x_3 = x'(t). \tag{A.4}$$

This yields

$$x_1' = 1, \quad x_2' = x_3, \quad x_3' = f(x_1, x_2, x_3). \tag{A.5}$$

Define vectors $X = (x_1, x_2, x_3)^T$, $F(X) = (1, x_3, f(x_1, x_2, x_3))^T$ and $A = (a, \alpha, \beta)^T$. This gives an initial value problem for X in vector form

$$X' = F(X), \quad X(a) = A. \tag{A.6}$$

One of the methods to solve the initial value problem is the fourth-order Runge Kutta method in vector form given by

$$X(t + h) = X(t) + \frac{1}{6}(F_1 + 2F_2 + 2F_3 + F_4), \tag{A.7}$$

where

$$
\begin{aligned}
F_1 &= hF(X), \\
F_2 &= hF(X + \frac{1}{2}F_1), \\
F_3 &= hF(X + \frac{1}{2}F_2), \\
F_4 &= hF(X + F_3).
\end{aligned}
$$

A.2 Shooting Method for Boundary Value Problem

We find the numerical solution for the boundary value problem

$$x''(t) = f(t, x, x') \quad \text{for} \quad a \leq t \leq b, \tag{A.8}$$

$$F(a, x(a), x'(a)) = 0, \tag{A.9}$$

$$G(b, x(b), x'(b)) = 0. \tag{A.10}$$

Set $x'(a) = z$, where z is any number. Then by the secant method, we can find the solution $x(a)$ from Equation (A.9) expressed as $x(a) = s(z)$, which means $x(a)$ depends on z. We thus obtain an initial value problem

$$
\begin{aligned}
x''(t) &= f(t, x, x') \\
x(a) &= s(z), \quad x'(a) = z.
\end{aligned}
$$

By Runge Kutta Formula from A.1, we can find the solution for this initial value problem expressed by $X(t, z)$, which depends on z also. At the end $t = b$, we establish a function from (A.10) as

$$G(b, X(b, z), X_t(b, z)), \tag{A.11}$$

which is actually implicitly dependent on z. We need to find a proper z such that $G(b, X(b,z), X_t(b,z)) = 0$. We can borrow the idea from secant method again to solve this problem.

A.3 Sleign2 Method for Computing Eigenvalues of Regular Sturm-Liouville Problem

Sleign2 is a library routine to compute the eigenvalues of the SLP given the coefficient formulas [45]. In our problem, however, finding the eigenvalues is only part of the algorithm, and we need to compute them in each iteration. Additionally, we cannot obtain the exact coefficient formulas but only a discrete form for them. As a result, understanding Sleign2 method in detail and incorporating it into our algorithm become significant. We make a simple demonstration for this method below.

Consider the Regular SLP

$$-\frac{d}{dx}(p(x)\frac{du(x)}{dx}) + q(x)u(x) = \lambda\omega(x)u(x), \tag{A.12}$$

$$a_0u(R_I) + a_1u'(R_I) = 0, \tag{A.13}$$

$$b_0u(R_O) + b_1u'(R_O) = 0. \tag{A.14}$$

For any eigenvalue λ, we can find two functions $\theta(x)$ and $\rho(x)$ satisfying

$$\begin{aligned} u(x) &= \rho(x)\sin(\theta(x)), \\ p(x)u'(x) &= \rho(x)\cos(\theta(x)). \end{aligned} \tag{A.15}$$

This is the so called *prüfer transformation*. Plugging (A.15) into (A.12), we obtain

the differential equations for $\theta(x)$ and $\rho(x)$ as

$$\theta'(x) = \frac{1}{p(x)}\cos^2(\theta(x)) + (\lambda\omega(x) - q(x))\sin^2(\theta(x)), \tag{A.16}$$

$$\frac{\rho'(x)}{\rho(x)} = \frac{1}{2}(\frac{1}{p(x)} - \lambda\omega(x) + q(x))\sin(2\theta(x)). \tag{A.17}$$

(A.16) is an ordinary differential equation for $\theta(x)$ only. The boundary conditions are found to be

$$\theta(R_I) = -\arctan(\frac{a_1}{p(R_I)a_0}) \quad \text{for} \quad \theta(R_I) \in [0, \pi), \tag{A.18}$$

$$\theta(R_O) = -\arctan(\frac{b_1}{p(R_O)b_0}) + (n+1)\pi \quad \text{for} \quad \theta(R_O) - (n+1)\pi \in (0, \pi], \tag{A.19}$$

where $n = 0, 1, 2 \ldots$

Combining (A.16) and (A.18), we get a solution for $\theta(x)$ named as $\theta_L(x)$. Similarly, combining (A.16) and (A.19) generates another solution $\theta_R(x)$. Both of these two solutions are implicit functions of λ. For any fixed point $x^* \in [R_I, R_O]$, we define a function

$$\Gamma_n(\lambda) = \theta_L(x^*) - \theta_R(x^*). \tag{A.20}$$

If λ happens to be the n^{th} eigenvalue, then $\Gamma_n(\lambda) = 0$. Otherwise, it returns nonzero value. We can make use of Newton's method (or bisection method) to find the zero of (A.20). The iteration for Newton's method is set to be

$$\lambda_n^{(m+1)} = \lambda_n^{(m)} - \Gamma_n(\lambda_n^{(m)})(\frac{d\Gamma_n(\lambda_n^{(m)})}{d\lambda})^{-1}. \tag{A.21}$$

The only thing left is to find $\frac{d\Gamma_n(\lambda_n^{(m)})}{d\lambda} = (\theta_L)_\lambda(x^*) - (\theta_R)_\lambda(x^*)$, where $(\theta_L)_\lambda$ means derivative of θ_L with respect to λ and the same for $(\theta_R)_\lambda$. First we find $(\theta_L)_\lambda$, the detail of which is as follows.

In (A.16), only $\theta_L(x)$ is a function of λ. We differentiate this equation with respect to λ and it yields

$$(\theta_L)'_\lambda = -f(x)(\theta_L)_\lambda + \omega(x)\sin^2\theta_L, \tag{A.22}$$

where $f(x) = (\frac{1}{p(x)} - \lambda\omega_L(x) + q(x))sin(2\theta_L)$. (A.22) is a first order ordinary equation for $(\theta_L)_\lambda$. Furthermore, from (A.18) we find that the initial value for $(\theta_L)_\lambda$ at $x = R_I$ is 0. Solution for (A.22) is

$$(\theta_L)_\lambda(x) = e^{-\int_{R_I}^{x} 2f(\xi)d\xi} \int_{R_I}^{x} e^{\int_{R_I}^{\eta} 2f(\xi)d\xi}\omega(\eta)\sin^2(\theta(\eta))d\eta. \tag{A.23}$$

Similarly, we get

$$(\theta_R)_\lambda(x) = e^{-\int_{R_O}^{x} 2f(\xi)d\xi} \int_{R_O}^{x} e^{\int_{R_O}^{\eta} 2f(\xi)d\xi}\omega(\eta)\sin^2(\theta(\eta))d\eta. \tag{A.24}$$

Hence we find $\frac{d\Gamma_n(\lambda_n^{(m)})}{d\lambda}$ from (A.23) and (A.24).

We need an initial guess $\lambda_n^{(0)}$ for (A.21), which can be found by Newton's method from

$$\int_{RI}^{RO} \sqrt{\frac{\lambda_n^{(0)}\omega(x) - q(x)}{p(x)}}dx = (n+1)\pi. \tag{A.25}$$

A.4 Nelder-Mead Simplex Method for Function Minimization

The so called Nelder-Mead simplex method was published by Nelder and Mead in 1965 [51]. It is one of the most widely used direct search methods for minimization of scalar-valued unconstrained function . The method minimizes a function with multiple variables by using only function values without utilization of any gradient.

Simplex is a geometrical object with flat surfaces (or sides), whose number of vertexes is one more bigger than the dimension of space where the object relies. For

example, a simplex in a plane is a triangle; a simplex in the 3-dimensional space is a tetrahedron. If the space dimension is n, the corresponding simplex is called n-simplex. By definition, a n-simplex owns $n+1$ vertexes.

The general idea of Nelder-Mead simplex method minimizing a function $f(x)$, for $x \in R^n$, depends on the comparison of function values at the $n+1$ vertexes of a simplex. The vertex generating the largest function value is replaced by another newly admitted point producing smaller one. Four actions are utilized to search a new point (or points): reflection, expansion, contraction and shrinkage. Four constrained parameters ρ, χ, γ and σ are prescribed to reflect the extent of each of the actions respectively. A frequent use of the values is $\rho = 1$, $\chi = 2$, $\gamma = 1/2$ and $\sigma = 1/2$. The detailed algorithm and explanation are described as follows:

1. For the k-th iteration, order the $n+1$ vertexes of the simplex to be $x_1^{(k)}$, $x_2^{(k)}$, $x_3^{(k)} \cdots x_{n+1}^{(k)}$ such that

$$f(x_1^{(k)}) \leq f(x_2^{(k)}) \leq f(x_3^{(k)}) \cdots \leq f(x_{n+1}^{(k)}).$$

   If the standard error $\sqrt{\frac{1}{n}\sum_{i=1}^{n}(f(x_i^{(k)}) - \overline{y})^2} < \xi$, where $\overline{y} = \frac{1}{n}\sum_{i=1}^{n} f(x_i^{(k)})$ and ξ is the tolerance number, then stop; Otherwise, go to Step 2;

2. Perform a **reflection** of point $x_{n+1}^{(k)}$ with respect to the centroid of the other n points to form a reflection point

$$x_r = \overline{x} + \rho(\overline{x} - x_{n+1}^{(k)}),$$

   where $\overline{x} = \frac{1}{n}\sum_{i=1}^{n} x_i^{(k)}$ expressing the centroid of points $x_1^{(k)}$, $x_2^{(k)}$, $x_3^{(k)} \cdots x_n^{(k)}$. If $f(x_1^{(k)}) \leq f(x_r) < f(x_n^{(k)})$, accept x_r, discard $x_{n+1}^{(k)}$ to form a new simplex, and go to Step 1 for the next iteration. Otherwise, if $f(x_r) < f(x_1^{(k)})$, go to

Step 3, and if $f(x_r) \geq f(x_n^{(k)})$, go to Step 4.

3. Since $f(x_r) < f(x_1^{(k)})$, it implies that smaller function value may be found further away from the reflection point. Thus, perform an **expansion** to form an expansion point

$$x_e = \overline{x} + \chi(x_r - \overline{x}).$$

If $f(x_e) < f(x_r)$, accept x_e as a new vertex, discard $x_{n+1}^{(k)}$ to form a new simplex and go to Step 1 for the next iteration. If not, accept x_r as a new vertex, discard $x_{n+1}^{(k)}$ to form a new simplex and go to Step 1 for the next iteration;

4. Since $f(x_r) \geq f(x_n^{(k)})$, this means points further away from the centroid $\overline{x}$ produces larger function value, so a **contraction** is performed to form a contraction point

$$x_c = \overline{x} + \gamma(x^* - \overline{x}),$$

where $x^* = x_r$, if $f(x_r) \leq f(x_{n+1}^{(k)})$ (*contract outside*); $x^* = x_{n+1}^{(k)}$, if $f(x_r) > f(x_{n+1}^{(k)})$ (*contract inside*).

If $f(x_c) \leq f(x^*)$, accept x_c, discard x_{n+1} to form a new simplex and go to Step 1; If $f(x_c) > f(x^*)$, go to Step 5;

5. Since $f(x_c) > f(x^*)$, this meas a **shrinkage** inside the simplex is required for search smaller function values. Perform such action to form shrinkage points:

$$v_i = x_1^{(k)} + \sigma(x_i^{(k)} - x_1^{(k)}), \quad i = 2, 3 \cdots n+1.$$

The $n+1$ points $x_1^{(k)}$, v_2, $v_3 \cdots v_{(n+1)}$ form a new simplex. Then go to Step 1 for next iteration.

The converge of the method for $n = 2$ is proved in [50].